Correlation of Line-of-Sight Probabilities in Aerial-Terrestrial Communications: Modeling, Analysis, and Application

Lin Chen, *Graduate Student Member, IEEE*, Wentao Zhang, Mustafa A. Kishk, *Member, IEEE*, and Mohamed-Slim Alouini, *Fellow, IEEE*

***Abstract*—The line-of-sight (LoS) condition is important to the quality of wireless communications, especially for millimeter-wave (mmWave) communications which are more sensitive to blockages than typical radio frequency (RF) communications. Considering that one blockage would obstruct several channels simultaneously, recently, researchers have studied the correlation of LoS probabilities among multiple channels in the horizontal plane and shown its importance in system performance analysis. The main missing aspect of existing literature in this direction is that the heights of transceivers and blockages have not been considered in the analysis of the LoS correlation. However, the emerging hybrid cellular networks with unmanned aerial vehicles (UAVs) and reconfigurable intelligent surfaces (RISs) deployed at various altitudes necessitate the LoS analysis accounting for the vertical dimension. In this paper, using stochastic geometry, we formulate a novel joint-LoS-probability framework of two channels among three aerial/terrestrial devices to analyze the LoS correlation both in the horizontal and vertical dimensions. We derive the expression of the conditional and joint LoS probabilities. The proposed framework combines (i) accuracy (verified in simulation), (ii) generality (from adjustable parameters of the channels and environments), and (iii) fitting ability (from a cylindrical blockage model to a non-cylindrical blockage model). The numerical results show that the correlation is quite strong when the angle between the two communication channels is small, while it becomes weaker as this angle increases. Moreover, we introduce a potential application of the joint LoS probability in the optimal deployment of an aerial device. Compared to optimization based on the independence assumption of the LoS probabilities, the improvement in the coverage probability intuitively clarifies the advantage of the proposed joint-LoS-probability framework on the aerial-terrestrial network design.**

***Index Terms*—Joint line-of-sight (LoS) probability, blockage correlation, stochastic geometry, aerial-terrestrial communications, unmanned aerial vehicle (UAV) deployment.**

Manuscript received 13 April 2023; revised 1 August 2023 and 24 October 2023; accepted 21 November 2023. Date of publication 29 November 2023; date of current version 16 May 2024. This work was supported by the King Abdullah University of Science and Technology. The review of this article was coordinated by Dr. Cunhua Pan. *(Corresponding author: Mustafa A. Kishk.)*

Lin Chen is with the Department of Information Engineering, The Chinese University of Hong Kong (CUHK),, Hong Kong (e-mail: lin.chen@link.cuhk.edu.hk).

Wentao Zhang is with the University of Electronic Science and Technology of China (UESTC), Chengdu 611731, China (e-mail: zwt0024@163.com).

Mustafa A. Kishk is with the Department of Electronic Engineering, Maynooth University, W23 F2H6 Maynooth, Ireland (e-mail: mustafa.kishk@mu.ie).

Mohamed-Slim Alouini is with the Computer, Electrical, and Mathematical Sciences and Engineering (CEMSE) Division, King Abdullah University of Science and Technology (KAUST), Thuwal 23955-6900, Saudi Arabia (e-mail: slim.alouini@kaust.edu.sa).

Digital Object Identifier 10.1109/TVT.2023.3337423

I. Introduction

In THE context of 5G and 6G, the millimeter-wave (mmWave) communication is anticipated to support higher throughput and lower latency [1], [2]. The high sensitivity of mmWave to blockage effects usually requires line-of-sight (LoS) channels [3], which calls for accurate modeling of the LoS probability. Considering that an obstacle with non-negligible volume could block the LoS across several channels simultaneously, the correlation of the LoS probability among channels should be incorporated into the modelling [4], [5]. Moreover, with the advent of unmanned aerial vehicles (UAVs) and reconfigurable intelligent surfaces (RISs) [6], [7], the various altitudes of communication devices and obstacles play a key role in predicting the LoS condition. The correlated LoS modeling should also take the vertical dimension into account in the hybrid aerial-terrestrial communication system.

Consider the dependence of LoS probability among three geographically close devices at different altitudes, denoted by Q_0, Q_1, and Q_2. If we know that an LoS channel exists between Q_0 and Q_1, we can deduce that there are no blockages in this channel (from the perspective of the horizontal plane), or blockages are too low to block the channel (from the perspective of the vertical plane). Intuitively, an LoS channel is more likely to exist between Q_0 and Q_2 as well. The increased LoS probability between Q_0 and Q_2 after the knowledge of LoS existence between Q_0 and Q_1 naturally implies the correlation between channels. In fact, the communication scenarios of two channels/links among three nodes are quite common. For example, for a typical user in downlink, the serving link and the interfering link are not completely independent with respect to the LoS probability, especially for the links provided by the serving base station (BS) and the nearest interfering BS [5]. In addition, the cutting-edge technology, RIS, is capable of converting a direct non line-of-sight (NLoS) path into an indirect LoS path by creating cascaded channels between a BS and a user equipment (UE), i.e, BS-RIS-UE [8]. Due to the close distances among the associated BS, RIS and UE with the different altitudes, ignoring the LoS correlation between the cascade channels would lead to inaccurate performance

analysis. The potential correlation of LoS probabilities between channels indicates that we can not directly apply the existing LoS models to independently predict the LoS conditions of channels, as done in most prior works for the deployment of UAVs or RISs, e.g. [8], [9], [10], [11]. Motivated by the above, in this paper, we extend an existing LoS-probability model of a single channel between two nodes in [12] to a novel joint-LoS-probability model of two channels among three nodes. To the best of our knowledge, this is the first work to provide analytical modeling of the joint LoS probability in aerial-terrestrial channels with an emphasis on the correlation of blockage effects in both the vertical and horizontal dimensions.

A. Related Work

The model of the LoS probability has been widely discussed in literature, which can be divided into: (i) empirical methods, (ii) deterministic methods, and (iii) stochastic geometry-based analysis of independent/correlated blockage effects.

The *empirical LoS models* recommended in 3rd Generation Partnership Project (3GPP) TR 36.814-900 [13] and International Telecommunication Union (ITU)-R P.1410-5 [14] are based on the fitting of the measurement data of a specific environment, where the heights of the communication devices are limited. Clearly, the application of this model to various communications scenarios is restricted, especially to the emerging cellular network composed of aerial and ground devices [15], [16], [17], [18]. *Deterministic methods*, e.g. the ray-tracing [19], are based on extensive simulations in the 3D model of the real world. Therefore, the ray-tracing with high computational complexity is not suitable for the application which requires timely feedback of channel state information (CSI), e.g., the optimal deployment of the UAV [20], [21], [22].

Stochastic geometry-based analysis of independent blockage effects: Predicting LoS probability using tools of stochastic geometry which combines generality and simplicity has attracted much research interest [12], [23], [24], [25]. In [23], the air-to-ground LoS probability is parameterized with the three properties of the urban environment defined by ITU in [14] and the elevation angle between the low altitudes platforms and the user. The authors in [12] characterize the communication environment more finely by the density, average height, and size of buildings in the target area. Therefore, the developed model in [12] can be easily applied to various environments with the transceivers being located at the same/different heights, making it possible to analyze aerial equipment (generally placed at different altitudes). The frequency is further considered in [24], which derives the expression of the LoS probability as a function of the environment parameters (including sizes, heights, and orientations of buildings) and the frequency. Considering the same parameters of the environment and the channel as [24], ref. [25] uses machine learning to provide an approximate parametric model of the LoS probability, which greatly reduces the computational complexity. The results of the above models have good consistency with either the Monte Carlo simulation results or the ray-tracing results. It is worth noting that these works only focus on a single channel. The correlation of LoS probability has not been considered in the analysis of the network performance metrics, e.g., signal-to-interference plus noise ratio (SINR)-based coverage probability [26], [27].

Stochastic geometry-based analysis of correlated blockage effects: Recently, the correlated blockage effect has been studied using tools from stochastic geometry, where the blockages are modeled as line segments with random lengths and orientations, and the midpoints of blockages follow a Poisson Boolean process [4], [5], [28], [29]. Authors in [4] analyze the dependence of the blockages between two channels in order to study the macro-diversity in a cellular network, where a UE attempts to connect with two BSs. The results show that the independent LoS probability overestimates the macro-diversity gain compared with the dependent LoS probability. In [28], [29], the impact of the correlated blockages on the LoS between anchors and targets has been studied in localization networks. The authors in [5] reveal the correlation of the blockage effect between the serving link and each interfering link, and analyze its impact on the SINR of the 1D and 2D mmWave cellular networks, respectively. The above works consider the correlation of the blockage effect only in the horizontal plane, while ignoring the impact of the thickness and height of blockages. Generally, the blockages have non-negligible length, width, and height. Under the modeling of the blockages/obstacles with the shape of line segments, when the line segment-shaped obstacle is parallel to the link, the blockage effect of the obstacle is ignored; when an obstacle with a low height and the link is above the obstacle, the blockage effect of the low obstacle is overestimated. Nevertheless, in the hybrid network consisting of aerial/terrestrial transceivers, the vertical dimension (characterizing the height of transceivers and obstacles) is a crucial feature in the LoS model.

B. Contributions

In this paper, we study the correlation of the LoS probability of two channels among three outdoor nodes in aerial-terrestrial communications. In contrast to previous work, we characterize the LoS correlation in both the vertical and horizontal dimensions (from the top and side views). Moreover, we consider the thickness and the height of blockages, which are modeled as cylinders with random heights in the vertical plane and circular shapes in the horizontal plane. The main contributions of this work are listed as follows.

- We propose a novel framework to characterize 3D LoS correlation. First, we define an *LoS area* of a channel. The high blockages lying in this area are capable of obstructing the channel. We then define the overlap of the LoS areas of two channels as a *limited LoS area*, where the tall blockages can block both channels. We represent the correlation of the LoS probabilities by refining the distribution of the heights of blockages located within the limited LoS area. Using stochastic geometry, we first derive the expression of the *conditional LoS probability* and then obtain the expression of the *joint LoS probability* with a simple extra step. The proposed analytical framework can also be used to predict the joint NLoS probability and the probability that one channel is LoS and the other is NLoS.

- We show the accuracy and generality of the proposed framework. The high agreement between analytical results (considering LoS correlation) and simulation results verifies the accuracy. The gap between analytical results with and without independent assumption demonstrates the correlation of the LoS probabilities, thereby supporting the necessity of our work. Moreover, the adjustable parameters of channels and environments enable our model to be a useful analytical tool for a wide range of application scenarios.
- We show that the *cylindrical* blockages can effectively approximate *non-cylindrical* blockages. By adjusting the parameters of blockage shapes, we find that the results obtained from cylindrical blockages exhibit a high degree of consistency with non-cylindrical blockages with square shapes in the horizontal plane. We can expect that the insights gained from the simple cylinder modeling with non-directional nature are similar to those from other complex non-cylinder modeling with orientation-specific nature. Therefore, the cylinder-based model maintains a certain level of simplicity while providing as many insights as possible.
- We apply the proposed framework of the correlated LoS probability to optimize the position of an aerial user (i.e., surveillance UAV). Compared with the UAV deployment ignoring the correlation of the LoS probability, we show the coverage enhancement using the correlated-LoS-probability based optimization. The increased coverage probability clarifies the effectiveness of the accurate modeling of the LoS correlation on the aerial-terrestrial network design to improve the system performance.

The remainder of this paper is organized as follows. Section II introduces the existing LoS model for a single channel between two nodes and we extend it in Section III to model the joint LoS probabilities of two channels among three nodes. In Section IV, we analyze the conditional LoS probability to calculate the joint LoS probability. Then, we validate the accuracy, generality, and fitting ability of the proposed model in Section V by extensive Monte-Carlo simulations. One of the applications of the LoS correlation is discussed in Section VI, where we optimize the position of an aerial user (surveillance UAV) and evaluate the corresponding coverage performance. Finally, we conclude our work in Section VII. A summary of notations used in the paper is provided in Table I.

TABLE I
TABLE OF NOTATIONS

Notation	Description
$\mu_{\rm b}$; $\sigma_{\rm b}$	Parameters of the log-normal distribution
$r_{\rm b}$	Radius of cylinder blockages
$\Psi_{\rm b}$	A PPP modeling blockage locations
$\lambda_{\rm b}$	Density of $\Psi_{\rm b}$
Q_i	Outdoor aerial or terrestrial node/device/equipment
H_{Q_i}	Height of node Q_i, $i=0,1,2$
c_{Q_i}	Circle centered at Q_i with radius r_b, $i=0,1,2$
XO_0Y	Cartesian coordinate system with origin at O_0
UO_2V	Cartesian coordinate system with origin at O_2
D_i	Horizontal distance between Q_0 and Q_i, $i=1,2$
Q_0Q_1	Line segment between Q_0 and Q_1 in the horizontal plane
Q_0-Q_1	Straight line connecting Q_0 and Q_1 in the vertical plane

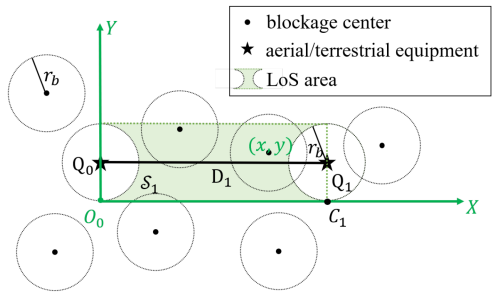

Fig. 1. Geometric illustration of the LoS condition of a single channel between two nodes in the horizontal dimension (from the top view).

II. Preliminaries of Geometrical LoS Condition

This section introduces an existing LoS model between nodes [12], as a preliminary for the extended joint LoS model.

We model the blockages, such as buildings, in the communication channels as cylinders with a fixed radius $r_{\rm b}$ and a random height $H>0$. The centers of the cylinders represent the locations of blockages and follow a Poisson point process (PPP) $\Psi_{\rm b}=\{b_i\}\in\mathbb{R}^2$ with a density of $\lambda_{\rm b}$. The cumulative distribution function (CDF) of the blockage height can be characterized by a log-normal distribution as [12]

$$F_H(h)=\mathbb{P}[H\le h]=\frac{1}{2}+\frac{1}{2}\,\mathrm{erf}\left[\frac{\ln h-\mu_{\rm b}}{\sqrt{2}\sigma_{\rm b}}\right], \quad (1)$$

where $\mu_{\rm b}$ and $\sigma_{\rm b}$ are the mean and standard deviation of the height logarithm. Fig. 1 presents the top view of the blockages and the channel between two nodes, Q_0 and Q_1, with altitudes H_{Q_0} and H_{Q_1}, respectively. Focusing on the outdoor communication setup, the circle centered at Q_0 (or Q_1) with radius $r_{\rm b}$, denoted as *outdoor region* c_{Q_0} (or c_{Q_1}), is excluded of any blockage centers.[1] Thus, we assume that the horizontal distance between Q_0 and Q_1, denoted by D_1, is greater than $2r_b$. In Fig. 1, we establish a Cartesian coordinate system XO_0Y, where the X-axis is parallel to line segment Q_0Q_1 in the horizontal plane and tangent to circles c_{Q_0} and c_{Q_1}. The tangent points are O_0 and C_1, respectively. Thus, points in c_{Q_0} satisfy the equation $x^2+(y-r_{\rm b})^2=r_{\rm b}^2$ and points in c_{Q_1} satisfy the equation $(x-D_1)^2+(y-r_{\rm b})^2=r_{\rm b}^2$. Note that the environment properties are characterized by four parameters, i.e., $\mu_{\rm b}$, $\sigma_{\rm b}$, $\lambda_{\rm b}$, and r_b [12]. To proceed, we define the LoS area between Q_0 and Q_1 as depicted in Fig. 1, denoted by $\mathcal{S}_1$, in the following.

Definition 1 (LoS area): An LoS area of the transceivers Q_0-Q_1 consists of a rectangular area (with width $2r_{\rm b}$, length D_1, and Q_0&Q_1 in its length axis) excluding two semicircles centered at Q_0 and Q_1, respectively. The blockages (with centers falling in the LoS area) intersect the line segment Q_0Q_1 in the horizontal plane. Only when no blockages in the LoS area obstruct the straight line connecting nodes Q_0 and Q_1 (i.e., Q_0-Q_1) in the 3D space, the geometrical LoS condition can be achieved.

[1] The outdoor assumption of equipment Q_0 and Q_1 necessitates the LoS analysis. If Q_0 and Q_1 are inside different buildings, the link between Q_0 and Q_1 is definitely NLoS.

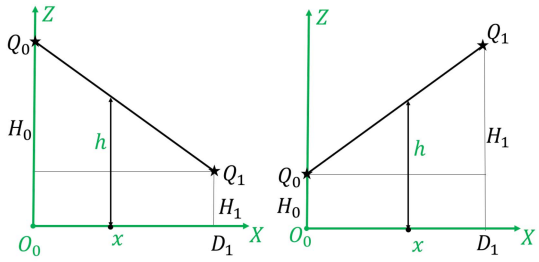

Fig. 2. Geometric illustration of the LoS condition in the vertical dimension (from the side view) for (a) $H_{Q_0} > H_{Q_1}$, (b) $H_{Q_0} \leq H_{Q_1}$.

It is clear that the blockages in the LoS area $\mathcal{S}_1$ affect the LoS condition between Q_0 and Q_1. As illustrated in Fig. 2, for LoS transmission, there is no blockages in $\mathcal{S}_1$ with the heights larger than the corresponding heights of points in the straight line Q_0-Q_1. Therefore, the probability of LoS between Q_0 and Q_1 is given by [12],

$$\mathcal{P}_L(Q_0, Q_1) = \mathbb{P}[\Psi_\mathrm{b} \cap \mathcal{S}_1 = \varnothing] = \exp(-\lambda_\mathrm{b} G_H(h)\,|\mathcal{S}_1|), \tag{2}$$

where $|\cdot|$ is the area measurement and $G_H(h)$ is the probability that the blockage height is larger than a predefined height h, which can be expressed by the complementary cumulative distribution function (CCDF) of the blockage height as

$$G_H(h) = \mathbb{P}[H > h] = 1 - \mathbb{P}[H \leq h] = 1 - F_H(h). \tag{3}$$

More specifically, it can be seen from Fig. 2 that, in the LoS area $\mathcal{S}_1$, the maximum allowable height of a blockage with a center located at (x, y) for the LoS transmission between Q_0 and Q_1 is given by [12]

$$h_{Q_0Q_1}(x) = \begin{cases} (H_{Q_0} - H_{Q_1})\frac{D_1 - x}{D_1} + H_{Q_1}, & \text{if } H_{Q_0} > H_{Q_1}, \\ (H_{Q_1} - H_{Q_0})\frac{x}{D_1} + H_{Q_0}, & \text{otherwise.} \end{cases} \tag{4}$$

By taking the event that the blockage is higher than the maximum allowable height as a mark on each blockage point and using ideas from the marked point process, (2) can be expressed in XO_0Y coordinate system as [30, Sec. 7.2]

$$\begin{aligned} \mathcal{P}_L(Q_0, Q_1) &= \exp\left(-\lambda_\mathrm{b} \int_{\mathcal{S}_1} G_H\left(h_{Q_0Q_1}(x)\right)\, \mathrm{d}\mathcal{S}\right) \\ &= \exp\left(-\lambda_\mathrm{b} \int_0^{2r_\mathrm{b}} \int_{c^+_{Q_0}(y)}^{c^-_{Q_1}(y)} G_H\left(h_{Q_0Q_1}(x)\right)\, \mathrm{d}x\, \mathrm{d}y\right), \end{aligned} \tag{5}$$

where $c^+_{Q_0}(y) = \sqrt{r_\mathrm{b}^2 - (y - r_\mathrm{b})^2}$ and $c^-_{Q_1}(y) = -\sqrt{r_\mathrm{b}^2 - (y - r_\mathrm{b})^2} + D_1$. It is worth noting that Q_0 and Q_1 can be any aerial or terrestrial device. Therefore, the scenarios in Fig. 2 for $H_{Q_0} > H_{Q_1}$ and $H_{Q_0} \leq H_{Q_1}$ are both possible, which however does not affect the top view in Fig. 1, i.e., the integration area $\mathcal{S}_1$ in (5) is same for the two scenarios.

III. Modeling of LoS Correlation

In this section, we add a new communication device (denoted by Q_2) into the basic modeling in Section II. Then, we analyze the probability that both Q_0-Q_1 channel and Q_0-Q_2 channel satisfy the LoS condition, i.e., joint LoS probability. By decomposing the joint LoS probability into the product of conditional and marginal LoS probabilities, we analyze the LoS correlation between channels Q_0-Q_1 and Q_0-Q_2. For the simplicity of illustration, we define the node Q_0 connecting two channels as *Tx*, and the other two nodes Q_1 and Q_2 as *Rxs*.

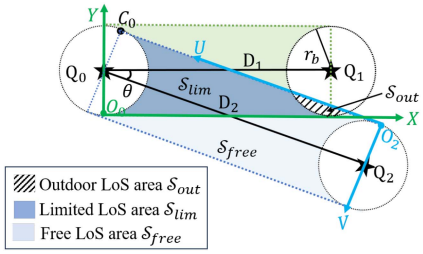

Fig. 3. Geometric illustration of the joint LoS condition of two channels among three nodes in the horizontal dimension (from the top view).

The new node Q_2 is with height H_{Q_2} and horizontal distance D_2 to Q_0. Also, Q_2 is assumed to be an outdoor device and $D_2 > 2r_b$, i.e., there is no blockage center falling in the circle centered at Q_2 with radius r_b, denoted by c_{Q_2}. We define the LoS area between Q_0 and Q_2 as $\mathcal{S}_2$. Besides, as shown in Fig. 3, the included angle between line segments Q_0Q_1 and Q_0Q_2 in the horizontal plane is annotated as $\theta \in [0, \pi]$. Let LoS_1 (or LoS_2) denote the event that the channel between Q_0 and Q_1 (or Q_2) is LoS. Then, *joint LoS probability* $\mathbb{P}(\mathrm{LoS}_1, \mathrm{LoS}_2)$ can be expressed by multiplying *conditional LoS probability* $\mathbb{P}(\mathrm{LoS}_2|\mathrm{LoS}_1)$ by *marginal LoS probability* $\mathbb{P}(\mathrm{LoS}_1)$, i.e.,

$$\mathbb{P}(\mathrm{LoS}_1, \mathrm{LoS}_2) = \mathbb{P}(\mathrm{LoS}_2|\mathrm{LoS}_1)\mathbb{P}(\mathrm{LoS}_1), \tag{6}$$

where $\mathbb{P}(\mathrm{LoS}_1) = \mathcal{P}_L(Q_0, Q_1)$ can be calculated by (5). In existing literature, the LoS probabilities of Q_0-Q_1 channel and Q_0-Q_2 channel are assumed to be independent as

$$\mathbb{P}(\mathrm{LoS}_1, \mathrm{LoS}_2) \approx \mathbb{P}(\mathrm{LoS}_2)\mathbb{P}(\mathrm{LoS}_1), \tag{7}$$

where $\mathbb{P}(\mathrm{LoS}_2) = \mathcal{P}_L(Q_0, Q_2)$ will be given later in (16). In contrast to the *independence approximation* in (7) using *unconditional LoS probability* $\mathbb{P}(\mathrm{LoS}_2)$, we consider the LoS *correlation* in (6) with respect to the conditional LoS probability $\mathbb{P}(\mathrm{LoS}_2|\mathrm{LoS}_1)$. In the following, we analyze the LoS probability between Q_0 and Q_2 under the condition that LoS transmission between Q_0 and Q_1 is known, i.e., $\mathbb{P}(\mathrm{LoS}_2|\mathrm{LoS}_1)$.

The impact of event LoS_1 on event LoS_2 can be observed from Fig. 3. First, there is an overlapping area between the LoS area $\mathcal{S}_2$ and the outdoor region, c_{Q_1}, denoted by $\mathcal{S}_{out} = \mathcal{S}_2 \cap c_{Q_1}$, termed as *outdoor LoS area*. Considering the outdoor communication in Section II, no blockage center falls in an outdoor region of any device. Hence, the probability that the blockage height is larger than a predefined height h in $\mathcal{S}_{out}$, denoted by $G_{out}(h)$, is 0. Hence, the LoS probability in $\mathcal{S}_{out}$, denoted by $\mathcal{P}_{out}$, equals to 1, which is from

$$\begin{aligned} \mathcal{P}_{out} &= \exp(-\lambda_\mathrm{b} G_{out}(h)\,|\mathcal{S}_{out}|) \\ &= \exp\left(-\lambda_\mathrm{b} \int_{\mathcal{S}_{out}} G_{out}(h)\, \mathrm{d}\mathcal{S}\right) = 1. \end{aligned} \tag{8}$$

Second, there is an overlapping area between the LoS areas $\mathcal{S}_2$ and $\mathcal{S}_1$, denoted by $\mathcal{S}_{lim}$, termed as *limited LoS area*, i.e., $\mathcal{S}_{lim} = \mathcal{S}_1 \cap \mathcal{S}_2$. The rest of the LoS area in $\mathcal{S}_2$ is denoted by $\mathcal{S}_{free}$, termed as *free LoS area*, where $\mathcal{S}_2 = \mathcal{S}_{out} \cup \mathcal{S}_{lim} \cup \mathcal{S}_{free}$. As discussed in Section II, the blockage height is limited by the maximum allowable height defined by the transceivers for LoS transmission. Namely, if there exist a LoS channel between Q_0 and Q_1, the blockage height, H, in the LoS area $\mathcal{S}_1$, satisfies $H \leq h_{Q_0Q_1}(x)$. Therefore, if LoS_1 happens, the blockage height in $\mathcal{S}_{lim}$ is limited by $h_{Q_0Q_1}(x)$, while it is still random with a distribution of (1) in $\mathcal{S}_{free}$. The following definitions provide the details of the three types of LoS area.

Definition 2 (Outdoor LoS area): The outdoor LoS area overlaps a LoS area and an outdoor region. There is no blockage center in the outdoor LoS area, i.e., the corresponding LoS probability is 1.

Definition 3 (Limited LoS area): The limited LoS area is the overlapping area between two LoS areas. When the LoS transmission in one of the channels is known, the blockage height in the limited LoS area is random but limited by the maximum allowable height for the known LoS channel.

Definition 4 (Free LoS area): The free LoS area is the LoS area excluding the limited and outdoor LoS areas. The blockage height in the free LoS area is randomly and independently distributed, which follows the log-normal distribution $F_H(h)$ in (1).

We notice that the maximum allowable height ($h_{Q_0Q_1}$) changes within the straight line between Q_0 and Q_1, while it remains the same value in the vertical direction of the line segment Q_0Q_1 (i.e., Y-axis), as shown in (4). Thus, $h_{Q_0Q_1}$ can be simply expressed as (4) with a single variable x in the established XO_0Y coordinate system. For analytical tractability, we consider another Cartesian coordinate system UO_2V in Fig. 3 to express the maximum allowable height between Q_0 and Q_2, where the U-axis is parallel to line segment Q_0Q_2 in the horizontal plane and tangent to circles c_{Q_2} and c_{Q_0}. The corresponding tangent points are O_2 and C_0, respectively. Therefore, points in c_{Q_2} satisfy the equation $u^2 + (v - r_\text{b})^2 = r_\text{b}^2$. For a specific point (x, y) in XO_0Y coordinate system, its equivalent coordinate in UO_2V coordinate system, i.e., (u, v), can be expressed as

$$\begin{bmatrix} u \\ v \\ 1 \end{bmatrix} = \begin{bmatrix} 1 & 0 & u_x \\ 0 & 1 & v_y \\ 0 & 0 & 1 \end{bmatrix} \begin{bmatrix} \cos\theta' & \sin\theta' & 0 \\ -\sin\theta' & \cos\theta' & 0 \\ 0 & 0 & 1 \end{bmatrix} \begin{bmatrix} x \\ y \\ 1 \end{bmatrix}, \quad (9)$$

where $\theta' = \pi - \theta$, $u_x = D_2 - r\sin\theta$, and $v_y = r_\text{b} + r_\text{b}\cos\theta$. Similar to (4), there are two possible settings: (i) one aerial Tx and two terrestrial Rxs (referred to as *A2T*) with $H_{Q_0} > H_{Q_1}$ and $H_{Q_0} > H_{Q_2}$, and (ii) one terrestrial Tx and two Rxs (referred to as *T2A*) with $H_{Q_0} \leq H_{Q_1}$ and $H_{Q_0} \leq H_{Q_2}$. Thus, the maximum allowable height of a blockage with a center located at (u, v) for LoS transmission between Q_0 and Q_2 is given under UO_2V coordinate system as

$$h_{Q_0Q_2}(u) = \begin{cases} (H_{Q_0} - H_{Q_2})\frac{D_2 - u}{D_2} + H_{Q_2}, & \text{if } H_{Q_0} > H_{Q_2}, \\ (H_{Q_2} - H_{Q_0})\frac{u}{D_2} + H_{Q_0}, & \text{otherwise.} \end{cases} \quad (10)$$

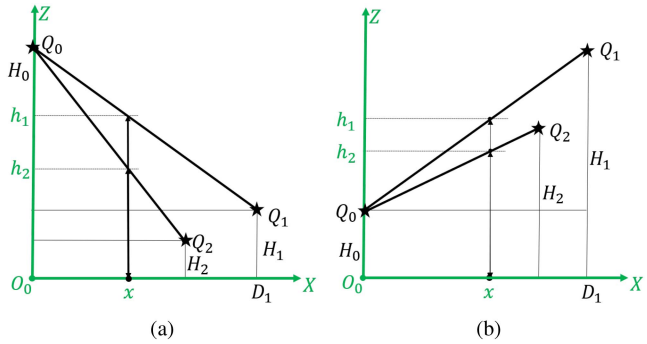

Fig. 4. Geometric illustration of the joint LoS condition in the vertical dimension (from the side view) for (a) T2A:$H_{Q_0} > H_{Q_1}$ and $H_{Q_0} > H_{Q_2}$ and (b) A2T:$H_{Q_0} \leq H_{Q_1}$ and $H_{Q_0} \leq H_{Q_2}$.

The LoS probability in $\mathcal{S}_{free}$, denoted by $\mathcal{P}_{free}$, can be calculated by following the same approach in (2) and (5) as

$$\begin{aligned} \mathcal{P}_{free} &= \exp(-\lambda_\text{b} G_{free}(h)\,|\mathcal{S}_{free}|) \\ &= \exp\left(-\lambda_\text{b} \int_{\mathcal{S}_{free}} G_H\left(h_{Q_0Q_2}(u)\right)\,\mathrm{d}\mathcal{S}\right). \end{aligned} \quad (11)$$

In Fig. 4, for a specific blockage center (x, y) at $\mathcal{S}_{lim}$ with a random height of $H > 0$, its maximum allowable height for the LoS Q_0-Q_1 channel is denoted by h_1, and for the LoS Q_0-Q_2 channel is denoted by h_2. Under the condition of the known LoS Q_0-Q_1 channel, it is clear that $H \leq h_1$ at $\mathcal{S}_{lim}$. Therefore, when $h_2 \geq h_1$, $H \leq h_2$ is naturally satisfied and this blockage does not act as the obstacle in the Q_0-Q_2 channel. i.e, $\mathbb{P}[H \leq h_2 | H \leq h_1] = 1$. While when $h_2 < h_1$ (as illustrated in Fig. 4), the probability that this blockage obstructs the straight line Q_0-Q_2 is given by

$$\begin{aligned} \mathbb{P}[H > h_2 | H \leq h_1] &= 1 - \frac{\mathbb{P}[H \leq h_2, H \leq h_1]}{\mathbb{P}[H \leq h_1]} \\ &= 1 - \frac{F_H(h_2)}{F_H(h_1)}. \end{aligned} \quad (12)$$

Therefore, the CCDF of the conditional blockage height in $\mathcal{S}_{lim}$ is given by

$$\begin{aligned} G_{lim}(h_2|h_1) &= \mathbb{P}[H > h_2 | H \leq h_1] \\ &= \begin{cases} 0, & h_2 \geq h_1, \\ 1 - \frac{F_H(h_2)}{F_H(h_1)}, & h_2 < h_1. \end{cases} \end{aligned} \quad (13)$$

From (2), the LoS probability in the limited area, denoted by $\mathcal{P}_{lim}$, can be written as

$$\mathcal{P}_{lim} = \exp(-\lambda_\text{b} G_{lim}(h_2(x,y)|h_1(x))\,|\mathcal{S}_{lim}|). \quad (14)$$

Specifically, in the limited LoS area, for a blockage located at (x, y) in XO_0Y coordinate system or (u, v) in UO_2V coordinate system, the maximum allowable height between Q_0 and Q_1 is $h_1(x) = h_{Q_0Q_1}(x)$, and the maximum allowable height between Q_0 and Q_2 is $h_2(x, y) = h_{Q_0Q_2}(u)$, where the transformation between $h_2(x, y)$ and $h_{Q_0Q_2}(u)$ is based on (9). Thus, the conditional LoS probability between Q_0 and Q_2 (conditioned on

TABLE II
SUMMARY OF GEOMETRICAL POINTS

Points	Description
O_0; O_2	The origin of the Cartesian coordinate systems XO_0Y or UO_2V
M_0	The intersection of the U-axis and the X-axis
C_0	The tangent point between the U-axis and circle c_{Q_1}
C_0'	C_0' is obtained by moving point C_0 upward along the V-axis by a length of $2r_\mathrm{b}$
C_2	The left intersection of circle c_{Q_2} and the X-axis
O_2'	Another intersection of circle c_{Q_2} and the line through O_2 and parallel to the X-axis, if present
M_1; M_1'	The left and right intersections of the X-axis and circle c_{Q_1}
C_{12}; C_{12}'	The left and right intersections of circles c_{Q_1} and c_{Q_2}

the known LoS Q_0-Q_1 channel) is

$$\begin{aligned}\mathbb{P}(\mathrm{LoS}_2|\mathrm{LoS}_1) &= \mathcal{P}_L(Q_0,Q_2|Q_0,Q_1)\\ &= \exp\left(-\lambda_\mathrm{b}\sum_{\chi\in\{out,\,free,\,lim\}}\int_{\mathcal{S}_\chi} G_\chi\,\mathrm{d}\mathcal{S}\right)\\ &\overset{(a)}{=} \mathcal{P}_{out}\times\mathcal{P}_{free}\times\mathcal{P}_{lim}\\ &\overset{(b)}{=} \mathcal{P}_{free}\times\mathcal{P}_{lim},\end{aligned}\tag{15}$$

where (a) is from $\mathcal{S}_2=\mathcal{S}_{out}\cup\mathcal{S}_{free}\cup\mathcal{S}_{lim}$ and the independence of three types of LoS areas, $G_\chi(\cdot)$ ($\chi\in\{free,\,lim,\,out\}$) is given in (8), (11), and (13), respectively, and (b) is from $\mathcal{P}_{out}=1$ in (8). From (15), the calculation of $\mathbb{P}(\mathrm{LoS}_2|\mathrm{LoS}_1)$ depends on $\mathcal{P}_{free}$ and $\mathcal{P}_{lim}$, which will be derived in the next section. On the other hand, similar to (5), the unconditional probability $\mathbb{P}(\mathrm{LoS}_2)$ in (7) can be calculated in UO_2V coordinate system as

$$\begin{aligned}\mathbb{P}(\mathrm{LoS}_2) &= \mathcal{P}_L(Q_0,Q_2) = \exp\left(-\lambda_\mathrm{b}\int_{\mathcal{S}_2} G_H\,\mathrm{d}\mathcal{S}\right)\\ &= \exp\left(-\lambda_\mathrm{b}\sum_{\chi\in\{out,\,free,\,lim\}}\int_{\mathcal{S}_\chi} G_H\,\mathrm{d}\mathcal{S}\right)\\ &= \exp\left(-\lambda_\mathrm{b}\int_0^{2r_\mathrm{b}}\int_{c^+_{Q_2}(v)}^{c^-_{Q_0}(v)} G_H\left(h_{Q_0Q_2}(u)\right)\,\mathrm{d}u\,\mathrm{d}v\right),\end{aligned}\tag{16}$$

where $c^+_{Q_2}(v)=\sqrt{r_\mathrm{b}^2-(v-r_\mathrm{b})^2}$ and $c^-_{Q_0}(v)=-\sqrt{r_\mathrm{b}^2-(v-r_\mathrm{b})^2}+D_2$. Comparing (15) with (16), the impact of LoS_1 on LoS_2 is manifested in the conditional blockage height within the limited LoS area, and no blockages in the outdoor LoS area, which implies that the independence approximation in (7) is not accurate.

IV. Analysis of Conditional and Joint LoS Probabilities

This section provides the mathematical expressions for the conditional LoS probability in (15). As discussed in (5), the relative heights of Q_1 and Q_2 with respect to Q_0 only affect the CCDF of the blockage height in (4) and (10), while have no effect on the integration areas $\mathcal{S}_{free}$ and $\mathcal{S}_{lim}$. Therefore, we provide the calculation of the integration areas in (11) and (14) without specifying the two settings in Fig. 4. Moreover, to simplify the analysis of $\mathcal{S}_{free}$ and $\mathcal{S}_{lim}$, we divide the calculation of the conditional LoS probability into two cases with respect to the included angle θ: (i) $\frac{\pi}{2}\le\theta\le\pi$ (obtuse&right angle) and (ii) $0\le\theta<\frac{\pi}{2}$ (acute angle). Finally, we introduce an extra step to obtain the exact joint LoS probability based on (6). Table II summarizes definitions of some points that are useful for subsequent analysis. For illustration, we take points C_1 and C_2 as an example. (U_{C_1},V_{C_1}) or (X_{C_1},Y_{C_1}) are the coordinates of C_1 in UO_2V or XO_0Y coordinate systems. $l_{C_1C_2}$ is the straight line through C_1 and C_2. Based on (9), Table III provides the coordinates of some points in XO_0Y and UO_2V coordinate systems, respectively, where $X_{M_0}=r_\mathrm{b}(\cos\theta+1)\cot\theta+r_\mathrm{b}\sin\theta$ and $U_{M_0}=-r_b(\cos\theta+1)\cot\theta+D_2-r_b\sin\theta$. In the following, $\mathcal{P}_{free}$ is calculated in UO_2V coordinate system and $\mathcal{P}_{lim}$ is calculated in XO_0Y coordinate system.

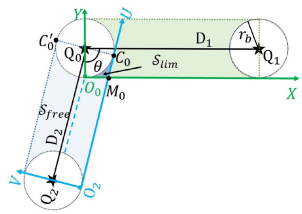

Fig. 5. Obtuse Angle.

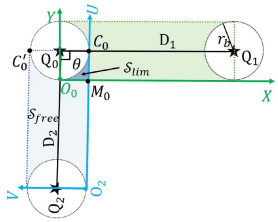

Fig. 6. Right Angle.

A. Obtuse&right Angle

Fig. 5 gives an example of the limited and free LoS areas between Q_0 and Q_2 when $\frac{\pi}{2}<\theta\le\pi$, where point M_0 is the intersection of the U-axis and the X-axis. The case of $\theta=\frac{\pi}{2}$ is shown in Fig. 6. From (11), the LoS probability in $\mathcal{S}_{free}$ can be

TABLE III
COORDINATES OF SOME POINTS IN XO_0Y AND UO_2V COORDINATE SYSTEMS

Points	O_0	M_0	C_0
(x, y)	$(0, 0)$	$(X_{M_0}, 0)$	$(r_\mathrm{b}\sin\theta, r_\mathrm{b}(\cos\theta+1))$
(u, v)	$(D_2 - r_\mathrm{b}\sin\theta, r_\mathrm{b}(1+\cos\theta))$	$(U_{M_0}, 0)$	$(D_2, 0)$
Points	O_2	Q_2	C_0'
(x, y)	$(D_2/\cos\theta, Y_{C_0} - D_2\sin\theta)$	$(D_2\cos\theta, r_\mathrm{b} - D_2\sin\theta)$	$(-r_\mathrm{b}\sin\theta, r_\mathrm{b}(1-\cos\theta))$
(u, v)	$(0, 0)$	$(0, r_\mathrm{b})$	$(D_2, 2r_\mathrm{b})$

expressed in UO_2V coordinate system as

$$\mathcal{P}_{free} = \exp\left(-\lambda_\mathrm{b}\left(\int_{V_{O_0}}^{2r_\mathrm{b}}\int_{c_{Q_2}^{+}(v)}^{c_{Q_0}^{-}(v)} G_H\left(h_{Q_0Q_2}(u)\right)\mathrm{d}u\,\mathrm{d}v + \int_{0}^{V_{O_0}}\int_{c_{Q_2}^{+}(v)}^{l_{M_0O_0}(v)} G_H\left(h_{Q_0Q_2}(u)\right)\mathrm{d}u\,\mathrm{d}v\right)\right), \tag{17}$$

where $c_{Q_2}^{+}(v)$ and $c_{Q_0}^{-}(v)$ are given in (16), $l_{M_0O_0}(v)$ is the equation of the straight line through M_0 and O_0, and $V_{O_0} = r_\mathrm{b}(1+\cos\theta)$ is the V-coordinate of point O_0. With the coordinates of M_0 and O_0 given in Table III, $l_{M_0O_0}(v)$ is given by

$$l_{M_0O_0}(v) = k_{M_0O_0}v + b_{M_0O_0},$$
$$k_{M_0O_0} = \frac{U_{M_0} - U_{O_0}}{V_{M_0} - V_{O_0}}, b_{M_0O_0} = U_{M_0} - k_{M_0O_0}V_{M_0}. \tag{18}$$

Note that $l_{M_0O_0}(v)$ is also the line equation of the X-axis in UO_2V coordinate system, denoted by $l_{XO_0}(v) = l_{M_0O_0}(v)$.

We next calculate the limited LoS probability in XO_0Y coordinate system from (14) as

$$\mathcal{P}_{lim} = \exp\left(-\lambda_\mathrm{b}\int_{0}^{Y_{C_0}}\int_{c_{Q_0}^{+}(y)}^{l_{M_0C_0}(y)} G_{lim}\left(h_2(x,y)|h_1(x)\right)\mathrm{d}x\,\mathrm{d}y\right), \tag{19}$$

where $Y_{C_0} = r_\mathrm{b}(\cos\theta+1)$ and $l_{M_0C_0}(y) = k_{M_0C_0}y + b_{M_0C_0}$ (with $k_{M_0C_0} = \frac{X_{M_0}-X_{C_0}}{Y_{M_0}-Y_{C_0}}$ and $b_{M_0C_0} = X_{M_0} - k_{M_0C_0}Y_{M_0}$). Also, the line equation of U-axis can be expressed as $l_{UO_2}(y) = l_{M_0C_0}(y)$.

B. Acute Angle

When $0 \le \theta < \frac{\pi}{2}$, we further divide this case into five scenarios based on the relative distances among D_1, D_2, and r_b, as illustrated in Fig. 7.

1) $2r_\mathrm{b} < D_2 < D_1 - R_\mathrm{b}$*:* In Fig. 8, point C_2/C_2' is the left/right intersection of circle c_{Q_2} and the X-axis, where $Y_{C_2} = Y_{C_2'} = 0$ and X_{C_2}/X_{C_2}' satisfies $(x - X_{Q_2})^2 + (Y_{C_2} - Y_{Q_2})^2 = r_\mathrm{b}^2$. The UO_2V coordinate of C_2 or C_2', i.e., (U_{C_2}, V_{C_2}) or $(U_{C_2'}, V_{C_2'})$, can be obtained based on (9). O_2' is another intersection of circle c_{Q_2} and the line through O_2 and parallel to the X-axis, where $Y_{O_2'} = Y_{O_2}$ and $X_{O_2'} = X_{O_2} - 2r_\mathrm{b}\sin\theta$. In Fig. 8(b), the origin of UO_2V coordinate system is right on the

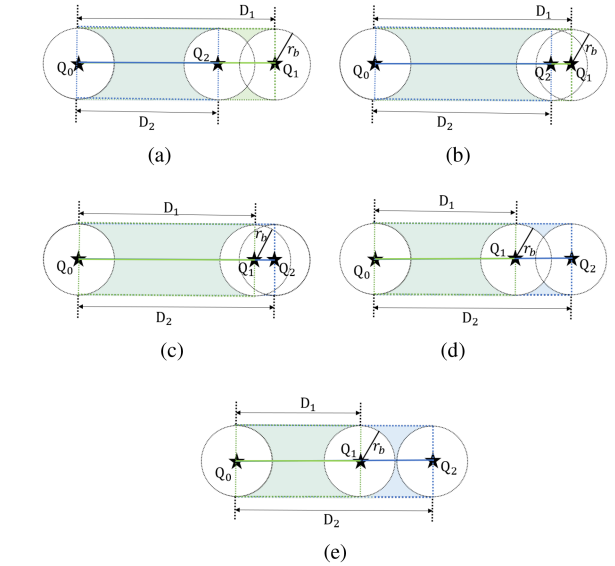

Fig. 7. Example of different scenarios for the case of $0 \le \theta < \frac{\pi}{2}$. (a) $2r_\mathrm{b} < D_2 < D_1 - r_\mathrm{b}$. (b) $D_1 - r_\mathrm{b} \le D_2 < D_1$. (c) $D_1 \le D_2 < D_1 + r_\mathrm{b}$. (d) $D_1 + r_\mathrm{b} \le D_2 < D_1 + 2r_\mathrm{b}$. (e) $D_1 + 2r_\mathrm{b} \le D_2$.

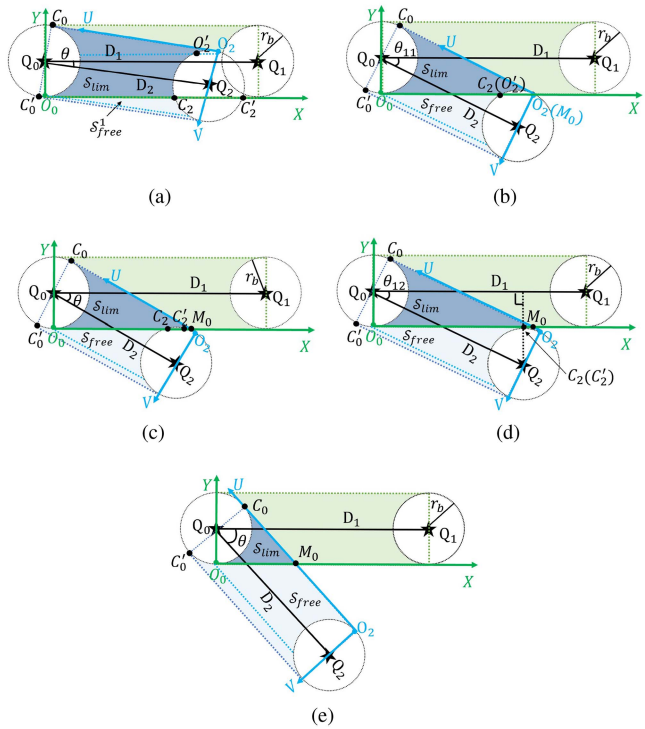

Fig. 8. Acute Angle for $2r_\mathrm{b} < D_2 < D_1 - r_\mathrm{b}$. (a) $0 \le \theta < \theta_{11}$. (b) $\theta = \theta_{11}$. (c) $\theta_{11} < \theta < \theta_{12}$. (d) $\theta = \theta_{12}$. (e) $\theta_{12} < \theta < \frac{\pi}{2}$.

X-axis and $\theta = \theta_{11}$ satisfies $Y_{O_2} = 0$, i.e., $r_{\mathrm{b}}(1+\cos\theta_{11}) - D_2 \sin\theta_{11} = 0$. In Fig. 8(d), circle c_{Q_2} is tangent to the X-axis, C_2 and C_2' coincide, and θ is denoted by θ_{12}, where $\sin\theta_{12} = \frac{2r_{\mathrm{b}}}{D_2}$.

For $0 \le \theta < \theta_{11}$ in Fig. 8(a), the free LoS probability is

$$\mathcal{P}_{free} = \exp\left(-\lambda_{\mathrm{b}}\left(\int_{V_{O_0}}^{2r_{\mathrm{b}}}\int_{c^+_{Q_2}(v)}^{c^-_{Q_0}(v)} G_H\left(h_{Q_0Q_2}(u)\right)\,\mathrm{d}u\,\mathrm{d}v + \int_{V_{C_2}}^{V_{O_0}}\int_{c^+_{Q_2}(v)}^{l_{XO_0}(v)} G_H\left(h_{Q_0Q_2}(u)\right)\,\mathrm{d}u\,\mathrm{d}v\right)\right), \tag{20}$$

where $c^+_{Q_2}(v)$ and $c^-_{Q_0}(v)$ are given in (16), and $l_{XO_0}(v) = l_{M_0O_0}(v)$ is given in (18). Particularly, we denote the free LoS area in Fig. 8(a) as $\mathcal{S}^1_{free}$ and the corresponding LoS probability as $\mathcal{P}^1_{free}$ given in (20). The limited LoS probability for $0 \le \theta < \theta_{11}$ is given by

$$\begin{aligned}\mathcal{P}_{lim} &= \exp\left(-\lambda_{\mathrm{b}}\left(\int_0^{Y_{O_2'}}\int_{c^+_{Q_0}(y)}^{c^-_{Q_2}(y)} G_{lim}\left(h_2(x,y)|h_1(x)\right)\,\mathrm{d}x\,\mathrm{d}y + \int_{Y_{O_2'}}^{Y_{C_0}}\int_{c^+_{Q_0}(y)}^{l_{UO_2}(y)} G_{lim}\left(h_2(x,y)|h_1(x)\right)\,\mathrm{d}x\,\mathrm{d}y - \int_{X_{O_2'}}^{X_{O_2}}\int_{Y_{O_2}}^{c^+_{Q_2}(x)} G_{lim}\left(h_2(x,y)|h_1(x)\right)\,\mathrm{d}y\,\mathrm{d}x\right)\right),\end{aligned} \tag{21}$$

where $c^-_{Q_2}(y) = -\sqrt{r_{\mathrm{b}}^2 - (y-Y_{Q_2})^2} + X_{Q_2}$, $c^+_{Q_2}(x) = \sqrt{r_{\mathrm{b}}^2 - (x-X_{Q_2})^2} + Y_{Q_2}$, and $l_{UO_2}(y) = l_{M_0C_0}(y)$ is given in (19).

For $\theta_{11} \le \theta < \theta_{12}$, we notice that the free LoS area (in Fig. 8(b) and (c)) includes the same shape as that in Fig. 8(a), i.e., $\mathcal{S}^1_{free}$. Thus, $\mathcal{P}_{free}$ can be expressed as

$$\begin{aligned}\mathcal{P}_{free} &= \exp\left(-\lambda_{\mathrm{b}}\int_{\mathcal{S}_{free}} G_H\left(h_{Q_0Q_2}(u)\right)\,\mathrm{d}\mathcal{S}\right)\\ &= \mathcal{P}^1_{free}\exp\left(-\lambda_{\mathrm{b}}\int_{\mathcal{S}_{free}\setminus\mathcal{S}^1_{free}} G_H\left(h_{Q_0Q_2}(u)\right)\,\mathrm{d}\mathcal{S}\right)\\ &= \mathcal{P}^1_{free}\exp\left(-\lambda_{\mathrm{b}}\int_0^{V_{C_2'}}\int_{c^+_{Q_2}(v)}^{l_{XO_0}(v)} G_H\left(h_{Q_0Q_2}(u)\right)\,\mathrm{d}u\,\mathrm{d}v\right),\end{aligned} \tag{22}$$

where $\mathcal{P}^1_{free}$ is given in (20). Similar to the second and third integration items in (21), $\mathcal{P}_{lim}$ in Fig. 8(b) and (c) is given by

$$\mathcal{P}_{lim} = \exp\left(-\lambda_{\mathrm{b}}\left(\int_0^{Y_{C_0}}\int_{c^+_{Q_0}(y)}^{l_{UO_2}(y)} G_{lim}\left(h_2(x,y)|h_1(x)\right)\,\mathrm{d}x\,\mathrm{d}y - \int_{X_{C_2'}}^{X_{C_2}}\int_0^{c^+_{Q_2}(x)} G_{lim}\left(h_2(x,y)|h_1(x)\right)\,\mathrm{d}y\,\mathrm{d}x\right)\right). \tag{23}$$

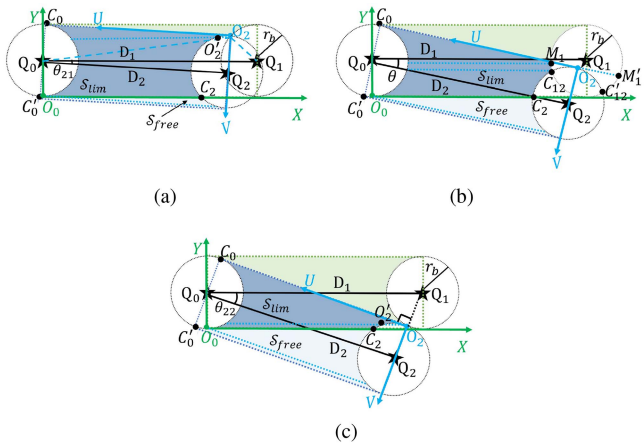

Fig. 9. Acute Angle for $D_1 - r_{\mathrm{b}} \le D_2 < D_1$. (a) $\theta = \theta_{21}$. (b) $\theta_{21} < \theta < \theta_{22}$. (c) $\theta = \theta_{22}$.

For $\theta_{12} \le \theta < \frac{\pi}{2}$ in Fig. 8(d) and (e), the LoS probability in the free area is given by

$$\mathcal{P}_{free} = \exp\left(-\lambda_{\mathrm{b}}\left(\int_{V_{O_0}}^{2r_{\mathrm{b}}}\int_{c^+_{Q_2}(v)}^{c^-_{Q_0}(v)} G_H\left(h_{Q_0Q_2}(u)\right)\,\mathrm{d}u\,\mathrm{d}v + \int_0^{V_{O_0}}\int_{c^+_{Q_2}(v)}^{l_{XO_0}(v)} G_H\left(h_{Q_0Q_2}(u)\right)\,\mathrm{d}u\,\mathrm{d}v\right)\right), \tag{24}$$

and the LoS probability in the limited area is given by

$$\mathcal{P}_{lim} = \exp\left(-\lambda_{\mathrm{b}}\int_0^{Y_{C_0}}\int_{c^+_{Q_0}(y)}^{l_{UO_2}(y)} G_{lim}\left(h_2(x,y)|h_1(x)\right)\,\mathrm{d}x\,\mathrm{d}y\right). \tag{25}$$

2) $D_1 - R_{\mathrm{b}} \le D_2 < D_1$: In Fig. 9, points C_{12} and C_{12}' are the left and right intersections of circles c_{Q_1} and c_{Q_2}, respectively, where $C_{12} = (X_{C_{12}}, Y_{C_{12}})$ and $C_{12} = (X_{C_{12}'}, Y_{C_{12}'})$ are the solutions of the following equation.

$$\begin{cases}(x-X_{Q_1})^2 + (y-Y_{Q_1})^2 &= r_{\mathrm{b}}^2,\\ (x-X_{Q_2})^2 + (y-Y_{Q_2})^2 &= r_{\mathrm{b}}^2,\end{cases} \tag{26}$$

where $X_{C_{12}} \le X_{C_{12}'}$. Points M_1 and M_1' are the left and right intersections of the U-axis and circle c_{Q_1}, respectively. The XO_0Y coordinates of M_1 and M_1' can be solved by the joint equation of circle c_{Q_1} and line l_{UO_2}, and then their corresponding UO_2V coordinates can be obtained from (9). In Fig. 9(a), O_2 is exactly the left intersection of circles c_{Q_1} and c_{Q_2}, and the angle between line $l_{Q_0Q_1}$ and line $l_{Q_0Q_2}$ is denoted by θ_{21} as

$$\begin{aligned}\theta_{21} &= \angle O_2Q_0Q_2 - \angle O_2Q_0Q_1\\ &= \arctan\frac{r_{\mathrm{b}}}{D_2} - \arccos\frac{D_1^2 + (D_2^2 + r_{\mathrm{b}}^2) - r_{\mathrm{b}}^2}{2D_1\sqrt{D_2^2 + r_{\mathrm{b}}^2}}.\end{aligned} \tag{27}$$

In Fig. 9(c), c_{Q_1} and c_{Q_2} are tangent to point O_2, the corresponding θ is marked as θ_{22}, where $\theta_{22} = \arctan\frac{2r_{\mathrm{b}}}{D_1}$.

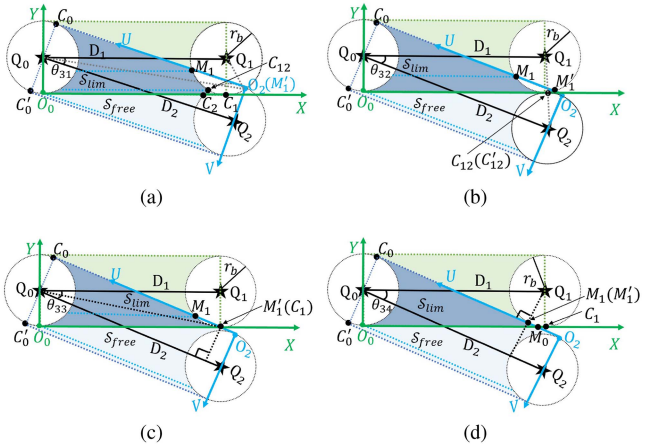

Fig. 10. Acute Angle for $D_1 \le D_2 < D_1 + r_\mathrm{b}$. (a) $\theta = \theta_{31}$. (b) $\theta = \theta_{32}$. (c) $\theta = \theta_{33}$. (d) $\theta = \theta_{34}$.

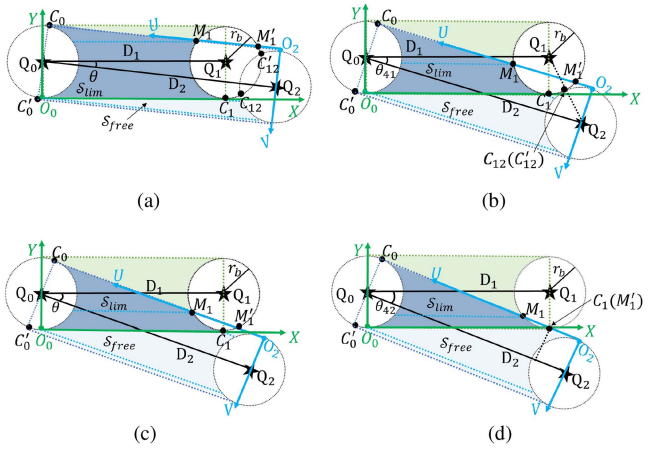

Fig. 11. Acute Angle for $D_1 + r_\mathrm{b} \le D_2 < D_1 + 2r_\mathrm{b}$. (a) $0 \le \theta < \theta_{41}$. (b) $\theta = \theta_{41}$. (c) $\theta_{41} < \theta < \theta_{42}$. (d) $\theta = \theta_{42}$.

For $0 \le \theta < \theta_{21}$, the shapes of integration areas are the same as that illustrated in Fig. 8(a). Thus, the corresponding LoS probability can be calculated by following the same way in (20) and (21).

For $\theta_{21} \le \theta < \theta_{22}$ in Fig. 9(a) and (b), the free LoS area is similar to $\mathcal{S}^1_{free}$ and thereby $\mathcal{P}_{free} = \mathcal{P}^1_{free}$, where $\mathcal{P}^1_{free}$ is given in (20). While the LoS probability in the limited LoS area is

$$\mathcal{P}_{lim} = \exp\Bigg(-\lambda_\mathrm{b} \Bigg(\int_0^{Y_{C_{12}}} \int_{c^+_{Q_0}(y)}^{c^-_{Q_2}(y)} G_{lim}\left(h_2(x,y)|h_1(x)\right)\,\mathrm{d}x\,\mathrm{d}y + \int_{Y_{C_{12}}}^{Y_{M_1}} \int_{c^+_{Q_0}(y)}^{c^-_{Q_1}(y)} G_{lim}\left(h_2(x,y)|h_1(x)\right)\,\mathrm{d}x\,\mathrm{d}y + \int_{Y_{M_1}}^{Y_{C_0}} \int_{c^+_{Q_0}(y)}^{l_{UO_2}(y)} G_{lim}\left(h_2(x,y)|h_1(x)\right)\,\mathrm{d}x\,\mathrm{d}y \Bigg)\Bigg). \quad (28)$$

For $\theta_{22} \le \theta < \frac{\pi}{2}$, we see that the following analysis is similar to that of Fig. 8(b)–(e), which thereby is omitted here.

3) $D_1 \le D_2 < D_1 + r_\mathrm{b}$*:* In Fig. 10(a), O_2 coincides with M_1' and the corresponding angle is denoted by θ_{31} as

$$\theta_{31} = \angle Q_1 Q_0 O_2 + \angle O_2 Q_0 Q_2 = \arccos \frac{D_1^2 + (D_1^2 + r_\mathrm{b}^2) - r_\mathrm{b}^2}{2D_1\sqrt{D_2^2 + r_\mathrm{b}^2}} + \arctan\frac{r_\mathrm{b}}{D_2}. \quad (29)$$

In Fig. 10(b), circles c_{Q_1} and c_{Q_2} are tangent to C_{12} (or C'_{12}) and $\theta_{32} = \arccos \frac{D_2^2 + D_1^2 - (2r_\mathrm{b})^2}{2D_2D_1}$. When M'_1 coincides with C_1 as shown in Fig. 10(c), the corresponding angle between $l_{Q_0Q_1}$ and $l_{Q_0Q_2}$ is marked as θ_{33}, where $\theta_{33} = 2\arctan\frac{r_\mathrm{b}}{D_1}$. In Fig. 10(d) where M_1 coincides with M'_1, i.e., circle c_{Q_1} is tangent to the U-axis, we denote θ as $\theta_{34} = \arcsin\frac{2r_\mathrm{b}}{D_1}$.

For $0 \le \theta < \theta_{31}$, the integration areas in Fig. 10(a) can be analyzed by following the same method to the analysis of Fig. 9(b) with (20) for $\mathcal{P}_{free}$ and (28) for $\mathcal{P}_{lim}$.

For $\theta_{31} \le \theta < \theta_{32}$, the free LoS probability is given by

$$\mathcal{P}_{free} = \mathcal{P}^1_{free} \times \exp\left(-\lambda_\mathrm{b} \int_0^{V_{C'_{12}}} \int_{c^+_{Q_2}(v)}^{c^-_{Q_1}(v)} G_H\left(h_{Q_0Q_2}(u)\right)\,\mathrm{d}u\,\mathrm{d}v \right), \quad (30)$$

and the limited LoS probability can be calculated by (28).

For $\theta_{32} \le \theta < \theta_{33}$, we have

$$\mathcal{P}_{free} = \exp\Bigg(-\lambda_\mathrm{b} \Bigg(\int_{V_{O_0}}^{2r_b} \int_{c^+_{Q_2}(v)}^{c^-_{Q_0}(v)} G_H\left(h_{Q_0Q_2}(u)\right)\,\mathrm{d}u\,\mathrm{d}v + \int_{V_{C_1}}^{V_{O_0}} \int_{c^+_{Q_2}(v)}^{l_{XO_0}(v)} G_H\left(h_{Q_0Q_2}(u)\right)\,\mathrm{d}u\,\mathrm{d}v + \int_0^{V_{C_1}} \int_{c^+_{Q_2}(v)}^{c^-_{Q_1}(v)} G_H\left(h_{Q_0Q_2}(u)\right)\,\mathrm{d}u\,\mathrm{d}v \Bigg)\Bigg), \quad (31)$$

$$\mathcal{P}_{lim} = \exp\Bigg(-\lambda_\mathrm{b} \Bigg(\int_0^{Y_{M_1}} \int_{c^+_{Q_0}(y)}^{c^-_{Q_1}(y)} G_{lim}\left(h_2(x,y)|h_1(x)\right)\,\mathrm{d}x\,\mathrm{d}y + \int_{Y_{M_1}}^{Y_{C_0}} \int_{c^+_{Q_0}(y)}^{l_{UO_2}(y)} G_{lim}\left(h_2(x,y)|h_1(x)\right)\,\mathrm{d}x\,\mathrm{d}y \Bigg)\Bigg). \quad (32)$$

For $\theta_{33} \le \theta < \theta_{34}$, we can obtain the free LoS probability by (24), and the calculation of the limited LoS probability is the same as in (32). For $\theta_{34} \le \theta < \frac{\pi}{2}$, the subsequent analysis is similar to that in Fig. 8(e). Therefore, we omit it here.

4) $D_1 + r_\mathrm{b} \le D_2 < D_1 + 2r_\mathrm{b}$*:* In Fig. 11(b), c_{Q_1} is tangent to c_{Q_2}, and thus $\theta_{41} = \theta_{32}$. In Fig. 11(d), C_1 coincides with M'_1, and thus $\theta_{42} = \theta_{33}$.

For $0 \le \theta < \theta_{41}$, the expression of the limited LoS probability is the same as (32). The free LoS probability is

$$\mathcal{P}_{free} = \exp\Bigg(-\lambda_{\mathrm{b}}\Bigg(\int_{V_{O_0}}^{V_{C_0'}}\int_{c_{Q_2}^{+}(v)}^{c_{Q_0}^{-}(v)} G_H\left(h_{Q_0Q_2}(u)\right)\,\mathrm{d}u\,\mathrm{d}v + \int_{V_{C_1}}^{V_{O_0}}\int_{c_{Q_2}^{+}(v)}^{l_{XO_0}(v)} G_H\left(h_{Q_0Q_2}(u)\right)\,\mathrm{d}u\,\mathrm{d}v + \int_{V_{C_{12}}}^{V_{C_1}}\int_{c_{Q_2}^{+}(v)}^{c_{Q_1}^{-}(v)} G_H\left(h_{Q_0Q_2}(u)\right)\,\mathrm{d}u\,\mathrm{d}v + \int_{0}^{V_{C_{12}'}}\int_{c_{Q_2}^{+}(v)}^{c_{Q_1}^{-}(v)} G_H\left(h_{Q_0Q_2}(u)\right)\,\mathrm{d}u\,\mathrm{d}v\Bigg)\Bigg). \tag{33}$$

When $\theta_{41} \le \theta < \frac{\pi}{2}$ and $D_1 + r_{\mathrm{b}} < D_2 \le D_1 + 2r_{\mathrm{b}}$ in Fig. 11, increasing θ changes the shape of the LoS areas, which is similar to that when $\theta \ge \theta_{32}$ with $D_1 < D_2 \le D_1 + r_{\mathrm{b}}$ in Fig. 10. Therefore, the following analysis is omitted.

5) $D_1 + 2r_{\mathrm{b}} \le D_2$: In this scenario, the analysis of the conditional LoS probability is similar to that of $D_1 + r_{\mathrm{b}} \le D_2 < D_1 + 2r_{\mathrm{b}}$ when $\theta \ge \theta_{41}$, which has been discussed in Section IV-B4.

C. Joint LoS Probability

This subsection introduces how to utilize the conditional LoS probability $\mathbb{P}(\mathrm{LoS}_2|\mathrm{LoS}_1)$ and the marginal LoS probability $\mathbb{P}(\mathrm{LoS}_1)$ to obtain the exact joint LoS probability, denoted by $\mathbb{P}^*(\mathrm{LoS}_1, \mathrm{LoS}_2)$.

Recall that in (6) we have decomposed $\mathbb{P}(\mathrm{LoS}_1, \mathrm{LoS}_2)$ into the product of $\mathbb{P}(\mathrm{LoS}_2|\mathrm{LoS}_1)$ and $\mathbb{P}(\mathrm{LoS}_1)$. Specifically, $\mathbb{P}(\mathrm{LoS}_2|\mathrm{LoS}_1)$ characterizes the dependence between LoS_1 and LoS_2, including the overlaps (i) between the LoS area $\mathcal{S}_2$ and the outdoor region c_{Q_1}, i.e., $\mathcal{S}_{out}$, and (ii) between the LoS areas $\mathcal{S}_2$ and $\mathcal{S}_1$, i.e., $\mathcal{S}_{lim}$. Based on (5), $\mathbb{P}(\mathrm{LoS}_1) = \mathcal{P}_L(Q_0, Q_1)$, which calculates the LoS probability over the whole LoS area $\mathcal{S}_1$. However, it can be observed from Fig. 7 that the outdoor region c_{Q_2} is possible to overlap the LoS area $\mathcal{S}_1$. Since there is no blockage center in the outdoor region, the exact LoS probability in $\mathcal{S}_1$ considering the existence of Q_2, denoted by $\mathbb{P}^*(\mathrm{LoS}_1)$, should be

$$\mathbb{P}^*(\mathrm{LoS}_1) = \exp\left(-\lambda_{\mathrm{b}}\int_{\mathcal{S}_1\setminus c_{Q_2}} G_H\left(h_{Q_0Q_1}(x)\right)\,\mathrm{d}\mathcal{S}\right) \ge \exp\left(-\lambda_{\mathrm{b}}\int_{\mathcal{S}_1} G_H\left(h_{Q_0Q_1}(x)\right)\,\mathrm{d}\mathcal{S}\right) = \mathbb{P}(\mathrm{LoS}_1), \tag{34}$$

where the equality holds if there is no overlap between $\mathcal{S}_1$ and c_{Q_2}, i.e., $\mathcal{S}_1 \cap c_{Q_2} = \varnothing$. Consequently, the exact joint LoS probability is

$$\mathbb{P}^*(\mathrm{LoS}_1, \mathrm{LoS}_2) = \mathbb{P}(\mathrm{LoS}_2|\mathrm{LoS}_1)\mathbb{P}^*(\mathrm{LoS}_1) \ge \mathbb{P}(\mathrm{LoS}_2|\mathrm{LoS}_1)\mathbb{P}(\mathrm{LoS}_1) = \mathbb{P}(\mathrm{LoS}_1, \mathrm{LoS}_2). \tag{35}$$

In the following, we show that when Q_1 is the nearest Rx to Tx Q_0 (i.e., $D_2 \ge D_1$), $\mathcal{S}_1$ does not overlap c_{Q_2}, thereby $\mathbb{P}^*(\mathrm{LoS}_1) = \mathbb{P}(\mathrm{LoS}_1)$.[2]

Notably, the overlap between c_{Q_2} and $\mathcal{S}_1$ happens when (i) the included angle θ between channels Q_0-Q_1 and Q_0-Q_2 is acute i.e., $\theta < 90°$, and (ii) the horizontal distance D_1 between Q_0 and Q_1 is greater than the horizontal distance D_2 between Q_0 and Q_2, i.e., $D_2 < D_1$. To be more specific, when $\theta \ge 90°$ with either $D_2 \ge D_1$ or $D_2 < D_1$ in Figs. 5 and 6, $c_{Q_2} \cap \mathcal{S}_1 = \varnothing$; when $\theta < 90°$ with $D_2 \ge D_1$ in Fig. 7(c)–(e), c_{Q_2} has almost no overlap with $\mathcal{S}_1$. Therefore, for any θ, when $D_2 \ge D_1$, $\mathbb{P}^*(\mathrm{LoS}_1) = \mathbb{P}(\mathrm{LoS}_1)$. However, when $\theta < 90°$ and $D_2 < D_1$ in Fig. 7(a)–(b), the overlap between c_{Q_2} and $\mathcal{S}_1$ is non-negligible, i.e., $\mathbb{P}^*(\mathrm{LoS}_1) \ne \mathbb{P}(\mathrm{LoS}_1)$, especially when θ is close to 0°.

To avoid the complex analysis of $\mathcal{S}_1 \setminus c_{Q_2}$ for calculating $\mathbb{P}^*(\mathrm{LoS}_1)$ in (34) when $D_2 < D_1$, there is an additional step before calculating the joint LoS probability. Consider one Tx T and two Rxs R_1 and R_2. The horizontal distance between T and R_1 (or R_2) is D_{TR_1} (or D_{TR_2}). The additional step is to set Tx T as Q_0, the 1st-closest Rx to Tx T as Q_1, and the 2nd-closest Rx to Tx T as Q_2. Thus, $D_1 = \min\{D_{TR_1}, D_{TR_2}\}$, which ensures $D_2 \ge D_1$ and then $\mathbb{P}^*(\mathrm{LoS}_1) = \mathbb{P}(\mathrm{LoS}_1)$. Specifically, there are two cases.

1) If $D_{TR_1} \le D_{TR_2}$, then set T, R_1, and R_2 as Q_0, Q_1, and Q_2, respectively, where $D_1 = D_{TR_1}$ and $D_2 = D_{TR_2}$. Therefore, $\mathbb{P}^*(\mathrm{LoS}_1) = \mathbb{P}(\mathrm{LoS}_1) = \mathcal{P}_L(Q_0, Q_1) = \mathcal{P}_L(T, R_1)$ and $\mathbb{P}(\mathrm{LoS}_2|\mathrm{LoS}_1) = \mathcal{P}_L(Q_0, Q_2|Q_0, Q_1) = \mathcal{P}_L(T, R_2|T, R_1)$.
2) If $D_{TR_1} > D_{TR_2}$, then set T, R_1, and R_2 as Q_0, Q_2, and Q_1, respectively, where $D_1 = D_{TR_2}$ and $D_2 = D_{TR_1}$. Therefore, $\mathbb{P}^*(\mathrm{LoS}_1) = \mathbb{P}(\mathrm{LoS}_1) = \mathcal{P}_L(Q_0, Q_1) = \mathcal{P}_L(T, R_2)$ and $\mathbb{P}(\mathrm{LoS}_2|\mathrm{LoS}_1) = \mathcal{P}_L(Q_0, Q_2|Q_0, Q_1) = \mathcal{P}_L(T, R_1|T, R_2)$.

Since $D_2 \ge D_1$, the equality in (35) holds, i.e.,

$$\begin{aligned}\mathbb{P}^*(\mathrm{LoS}_1, \mathrm{LoS}_2) &= \mathbb{P}(\mathrm{LoS}_2|\mathrm{LoS}_1)\mathbb{P}^*(\mathrm{LoS}_1)\\ &= \mathbb{P}(\mathrm{LoS}_1, \mathrm{LoS}_2) = \mathbb{P}(\mathrm{LoS}_2|\mathrm{LoS}_1)\mathbb{P}(\mathrm{LoS}_1)\\ &\overset{(a)}{=} \mathcal{P}_L(T, R_2|T, R_1)\mathcal{P}_L(T, R_1)\\ &\overset{(b)}{=} \mathcal{P}_L(T, R_1|T, R_2)\mathcal{P}_L(T, R_2).\end{aligned} \tag{36}$$

From (36), either by setting R_1 as Q_1 in case (a) or as Q_2 in case (b), the results of the joint LoS probability are the same. However, setting the 1st-closest Rx to Tx as Q_1 ensures $D_2 \ge D_1$. In this setting, $\mathbb{P}^*(\mathrm{LoS}_1) = \mathbb{P}(\mathrm{LoS}_1)$ can be easily obtained by (5) without analyzing the overlap between $\mathcal{S}_1$ and c_{Q_2}, which greatly simplifies the analysis of $\mathbb{P}^*(\mathrm{LoS}_1)$. Then, based on the analysis of $\mathbb{P}(\mathrm{LoS}_2|\mathrm{LoS}_1)$ for different values of θ, D_1, and D_2 in Section IV-B1-IV-B5. we can accurately calculate the joint LoS probability by (6).

[2]For more than two Rxs, $\mathbb{P}^*(\mathrm{LoS}_1) = \mathbb{P}(\mathrm{LoS}_1)$ is still true if Q_1 is the nearest Rx to Tx Q_0.

TABLE IV
DEFAULT VALUES OF MODEL PARAMETERS

Model parameters	Default values
$(\mu_{\rm b}, \sigma_{\rm b})$	$(1.12, 1.17)$
$r_{\rm b}$	30 m
$\lambda_{\rm b}$	5×10^{-4} blockages/m^2
$\lambda_{\rm T}$	5×10^{-5} TBSs/m^2
$(H_{Q_0}, H_{Q_1}, H_{Q_2}, h_{\rm T})$	$(100, 0, 0, 15)$ m
(D_1, D_2)	$(500, 580)$ m
$P_{\rm t}$	-6 dB
$G_{\rm t}$	10 dB
$(m_{\rm L}, m_{\rm N})$	$(3, 1)$
τ	-10 dB
$(\alpha_{\rm L}, \alpha_{\rm N})$	$(2.09, 3.75)$
$(\eta_{\rm L}, \eta_{\rm N})$	$(-32.9, -41.1)$ dB

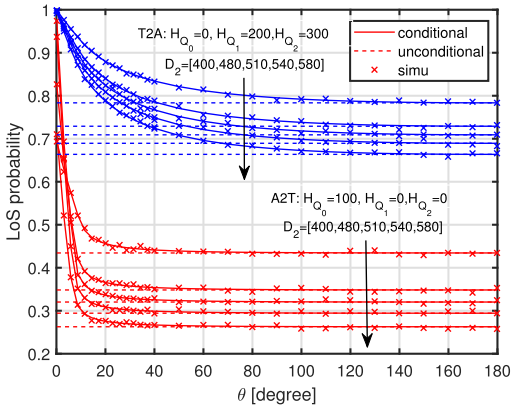

Fig. 12. Conditional and unconditional LoS probabilities, i.e., $\mathbb{P}(\mathrm{LoS}_2|\mathrm{LoS}_1)$ and $\mathbb{P}(\mathrm{LoS}_2)$, verified in two settings: (a) A2T with red lines and (b) T2A with blue lines.

V. MODEL VALIDATION: CONDITIONAL AND JOINT LOS PROBABILITY

In this section, we provide the numerical results of the derived expressions and the extensive Monte-Carlo simulation results. The default values of model parameters are summarized in Table IV, unless otherwise specified.

1) Monte-Carlo Simulations: Monte-Carlo simulations are considered for the system in a square area of $2 \times 2\,\mathrm{km}^2$, and the simulation results are obtained by averaging over 10^4 iterations. In each iteration, we generate a PPP $\Psi_b = \{b_i\}$ with density λ_b to model the randomly distributed blockages (in the shape of circles with radius r_b) in the horizontal plane. Considering the XO_0Y coordinate system with the origin at the center of the square area, we set $Q_0 = (0, r_b)$, $Q_1 = (D_1, r_b)$, $Q_2 = (D_2 \cos\theta, r_b - D_2 \sin\theta)$.

To obtain the simulation results of *marginal LoS probability* $\mathbb{P}(\mathrm{LoS}_1)$, we trace the straight line Q_0-Q_1 in 3D with the following steps in each iteration.

1) Generate the height h_i of each point $b_i \in \Psi_b$ based on the CCDF of the blockage height G_H in (3).
2) Collect all the blockage points falling in the LoS area $\mathcal{S}_1$.
3) Compute the maximum allowable height $h_{Q_0Q_1}(x)$ in (4).
4) For a blockage located at $b_i = (x, y) \in \mathcal{S}_1$ with height h_i, check whether $h_i \le h_{Q_0Q_1}(x)$.
5) If all blockage heights in $\mathcal{S}_1$ are lower than the maximum allowable height, mark this iteration as marginal LoS.

For *joint LoS probability* $\mathbb{P}(\mathrm{LoS}_1, \mathrm{LoS}_2)$, in each iteration, the steps (b)–(e) should be conducted in the LoS areas $\mathcal{S}_1$ and $\mathcal{S}_2$, respectively. When both Q_0-Q_1 and Q_0-Q_2 channels are LoS, we mark this iteration as a joint LoS iteration.

Different from steps (a) and (b), to simulate *conditional LoS probability* $\mathbb{P}(\mathrm{LoS}_2|\mathrm{LoS}_1)$, we first collect the blockage points falling in the limited and free LoS areas, $\mathcal{S}_{lim}$ and $\mathcal{S}_{free}$, respectively. Then, the heights of blockages falling in $\mathcal{S}_{lim}$ (or $\mathcal{S}_{free}$) are randomly generated based on G_{lim} in (13) (or G_{free} in (11)). Since there are no blockages in the outdoor LoS area $\mathcal{S}_{out}$, we compare the heights of blockages in $\mathcal{S}_{lim}$ and $\mathcal{S}_{free}$ with the maximum allowable height $h_{Q_0Q_2}(u)$. If any blockage $b_i = (u, v) \in \mathcal{S}_{lim} \cup \mathcal{S}_{free}$ with height h_i satisfies $h_i < h_{Q_0Q_2}(u)$, this iteration is marked as conditional LoS.

The estimated marginal/joint/conditional LoS probability is the number of marginal/joint/conditional LoS iterations divided by the total number of iterations.

2) Validation of Conditional LoS Probability: Fig. 12 plots the conditional LoS probability $\mathbb{P}(\mathrm{LoS}_2|\mathrm{LoS}_1)$ and the unconditional LoS probability $\mathbb{P}(\mathrm{LoS}_2)$ in two settings: (a) A2T: an aerial device (Q_0) and two terrestrial devices (Q_1 and Q_2), and (b) T2A: an terrestrial device (Q_0) and two aerial devices (Q_1 and Q_2). We increase the angle between line segments Q_0Q_1 and Q_0Q_2 from $\theta = 0^\circ$ to 180°. Additionally, fixing the horizontal distance between Q_0 and Q_1 as $D_1 = 500\,\mathrm{m}$, we change the horizontal distance between Q_0 and Q_2 ($D_2 \in \{400, 480, 510, 540, 580\}$) as five distance scenarios classified in Section IV-B. In Fig. 12, we see that the simulation results of $\mathbb{P}(\mathrm{LoS}_2|\mathrm{LoS}_1)$ closely match the corresponding analytical results in both two settings, which verifies the accuracy of the analysis in Section IV. Moreover, we notice that the heights of Q_0, Q_1, and Q_2 can be assigned any values to represent terrestrial, aerial, and terrestrial-aerial communications. Such flexibility enables an extensive range of applications in analyzing the LoS correlation in diverse cellular networks.

In the A2T setting of Fig. 12, we see that the gap between $\mathbb{P}(\mathrm{LoS}_2|\mathrm{LoS}_1)$ and $\mathbb{P}(\mathrm{LoS}_2)$, indicating the correlation of the LoS condition between channels Q_0-Q_1 and Q_0-Q_2. The gap becomes more obvious when θ and D_2 are relatively small. As depicted in Figs. 8–11, decreasing θ and D_2 makes Q_2 closer to Q_1. Consequently, the overlap between the LoS areas defined by Q_0-Q_1 and Q_0-Q_2 (i.e., the limited LoS area $\mathcal{S}_{lim}$) increases, implying that events LoS_1 and LoS_2 become more related. However, when Q_1 is far away from Q_2, the correlation of LoS_1 and LoS_2 is quite weak and even disappears since the blockages that affect the LoS condition of channel Q_0-Q_1 are almost/totally different from that of channel Q_0-Q_2. This explains why the curve of $\mathbb{P}(\mathrm{LoS}_2|\mathrm{LoS}_1)$ is asymptotic to the curve of $\mathbb{P}(\mathrm{LoS}_2)$ with the increasing values of θ. It can be expected that the joint LoS probability of more channels by considering more geometrical distant nodes would be much more complex; while

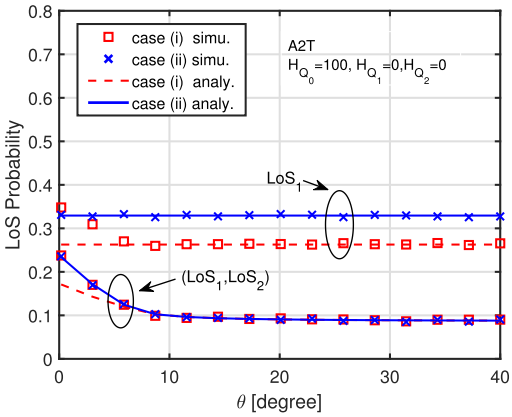

Fig. 13. Marginal and joint LoS probabilities, i.e., $\mathbb{P}(\mathrm{LoS}_1)$ and $\mathbb{P}(\mathrm{LoS}_1, \mathrm{LoS}_2)$. Consider three devices T, R_1, and R_2, with $D_{TR_1} = 580\,\mathrm{m} \geq D_{QR_2} = 500\,\mathrm{m}$ in two cases: (i) $Q_0 = T$, $Q_1 = R_1$, and $Q_2 = R_2$ with $D_2 < D_1$ and $\mathbb{P}(\mathrm{LoS}_1) = \mathcal{P}_L(T, R_1)$; (ii) $Q_0 = T$, $Q_1 = R_2$, and $Q_2 = R_1$ with $D_2 \geq D_1$ and $\mathbb{P}(\mathrm{LoS}_1) = \mathcal{P}_L(T, R_2)$.

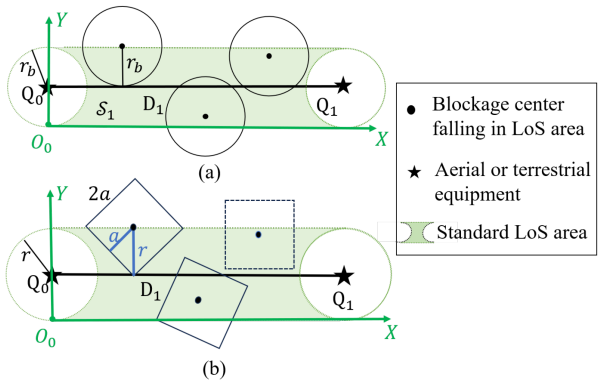

Fig. 14. Modeling blockages as circles vs squares in the horizontal plane.

the correlation might not be stronger. Therefore, in most cases, it is sufficient to consider the correlation of LoS probability between channels among three neighboring nodes.

Interestingly, comparing two settings in Fig. 12, we observe a notable discrepancy in the minimum angle at which the LoS correlation becomes negligible. Specifically, this angle is approximately 40° in the A2T setting, whereas it increases to 100° in the T2A setting. Hence, the strong LoS correlation should be incorporated into the analysis of aerial-terrestrial communications, especially for terrestrial-to-aerial channels.

3) Validation of Joint LoS Probability: Fig. 13 visualizes the disparity between $\mathbb{P}^*(\mathrm{LoS}_1)$ (or $\mathbb{P}^*(\mathrm{LoS}_1, \mathrm{LoS}_2)$) and $\mathbb{P}(\mathrm{LoS}_1)$ (or $\mathbb{P}(\mathrm{LoS}_1, \mathrm{LoS}_2)$) when $D_2 < D_1$, as well as the agreement between them when $D_2 \geq D_1$. Specifically, we consider a Tx T and two Rxs R_1 and R_2, where $D_{TR_1} = 580\,\mathrm{m} > \mathrm{D}_{\mathrm{TR}_2} = 500\,\mathrm{m}$. The simulation results correspond to the values of $\mathbb{P}^*(\mathrm{LoS}_1)$ and $\mathbb{P}^*(\mathrm{LoS}_1, \mathrm{LoS}_2)$. There are two cases: (i) $Q_0 = T, Q_1 = R_1$, and $Q_2 = R_2$ with $D_2 = D_{TR_2} < D_1 = D_{TR_1}$; and (ii) $Q_0 = T$, $Q_1 = R_2$, and $Q_2 = R_1$ with $D_2 = D_{TR_1} \geq D_1 = D_{TR_2}$. We can observe the high agreement between the simulation results of $\mathbb{P}^*(\mathrm{LoS}_1)$ and the analytical results of $\mathbb{P}(\mathrm{LoS}_1)$ in case (ii) with $D_2 \geq D_1$, i.e, $\mathbb{P}^*(\mathrm{LoS}_1) = \mathbb{P}(\mathrm{LoS}_1) = \mathcal{P}_L(T, R_2)$; while there is a gap between them in case (i) with $D_2 < D_1$, especially when θ is small, i.e., $\mathbb{P}^*(\mathrm{LoS}_1) \geq \mathbb{P}(\mathrm{LoS}_1) = \mathcal{P}_L(T, R_1)$. As discussed in Section IV-C, when $D_2 \geq D_1$, the overlap between c_{Q_2} and $\mathcal{S}_1$ results in the gap, which gradually reduces and finally disappears as θ increases. Moreover, in both cases, we can obtain the same simulation results of the joint LoS probability; while the analytical results of $\mathbb{P}(\mathrm{LoS}_1, \mathrm{LoS}_2)$ match the corresponding simulation results only in case (ii) with $D_2 \geq D_1$. These observations verify the effectiveness of the simple additional step (i.e., setting the closest Rx as Q_1) in Section IV-C to obtain the accurate joint LoS probability.

4) Model Fitting From Cylindrical to Non-Cylindrical Blockages: In Section II, we model blockages as cylinders in 3D or circles in the horizontal plane. The non-orientation nature of circles leads to the standard shape of the LoS area, e.g., the green shaded area $\mathcal{S}_1$ between Q_0 and Q_1 in Fig. 14(a). Any blockage center falling in $\mathcal{S}_1$ intersects with the line segment Q_0Q_1 and obstructs the Q_0-Q_1 channel if the blockage is higher than the straight line Q_0-Q_1 in the 3D space. However, for any non-cylindrical/non-circular model with a random orientation, it is possible that a blockage center within $\mathcal{S}_1$ has no impact on the LoS condition of Q_0-Q_1 channel, even if the blockage height is above the straight line Q_0-Q_1, e.g., the square with a dashed border in Fig. 14(b). Hence, both the locations and orientations of non-circular blockages are required to decide the LoS area, i.e., the LoS area is orientation-specific, which greatly complicates the analysis of the correlated LoS.

We take the square shape of blockages as an example. In Fig. 14, the side and diagonal lengths of a square are $2a$ and $2r$, respectively. Considering the random orientations of square blockages, we adopt the safest outdoor communication setup, i.e., the circle centered at Q_0 or Q_1 with radius $r = \sqrt{2}a$ does not contain any blockage center. The LoS area $\mathcal{S}_1$ under the circular blockage modeling is referred to as *standard LoS area*; while the LoS area under the square blockage modeling is referred to as *orientation-specific LoS area*, denoted by $\mathcal{S}_1'$. Therefore, the standard LoS area $\mathcal{S}_1$ consists of a rectangular area (with width $2r$, length D_1, and Q_0&Q_1 in its length axis) excluding two semicircles centered at Q_0 and Q_1. The orientation of a square, denoted by ϕ, is the angle between the line parallel to the y-axis and the perpendicular line from the center of the square to the side of the square. Due to the symmetry of the square, a square with direction $\phi = 0$ is the same as one with direction $\phi = \frac{\pi}{2}$. Hence, we assume that ϕ follows a uniform distribution over $[0, \frac{\pi}{2})$. It is clear that only when the square blockage intersects the line segment Q_0Q_1 in the horizontal plane, the square-blockage height is crucial for determining the LoS condition. Therefore, we need to check the position of the nearest square vertex to the line segment Q_0Q_1. As illustrated in Fig. 15, we can define the *orientation-specific LoS area* as $\mathcal{S}_1' = \{(x, y) : |y - r| \leq d = r\cos(\frac{\pi}{4} - \phi), (x, y) \in \mathcal{S}_1\}$. Following the similar steps in Section V-A1, we can generate the simulation results under the square blockage modeling. The difference is that we should compare the heights of blockage centers falling in $\mathcal{S}_1'$ (instead of $\mathcal{S}_1$) with the maximum allowable height $h_{Q_0Q_1}(x)$.

Fig. 16 compares the marginal and joint LoS probabilities obtained by modeling blockages as circles (with radius r_b) with

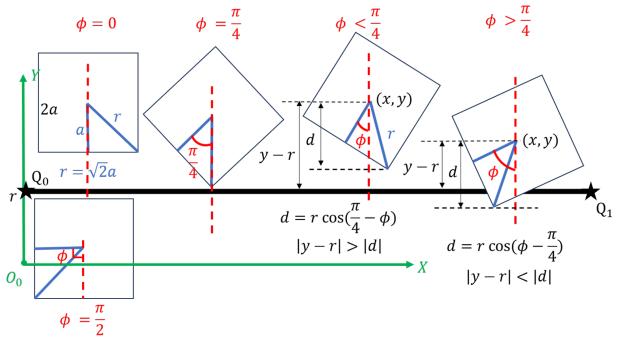

Fig. 15. Orientations of squares in the standard LoS area $\mathcal{S}_1$.

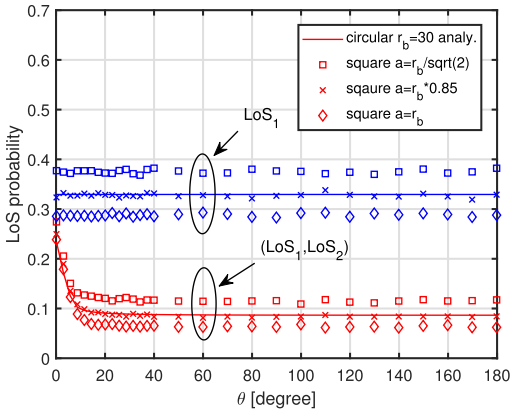

Fig. 16. Marginal and joint LoS probabilities under circular and square modeling of blockages in the horizontal plane, where r_b is the radius of a circle and a is the half side length of a square.

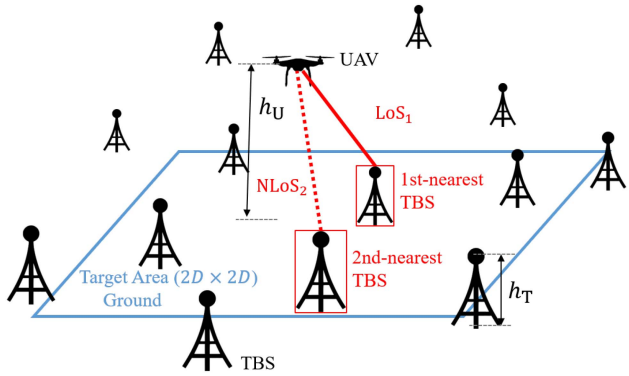

Fig. 17. Description of a cellular network with aerial-terrestrial communications.

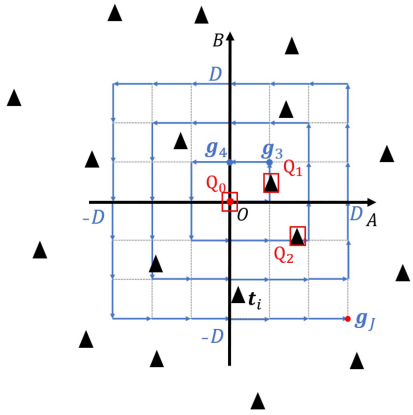

Fig. 18. Illustration of the optimal deployment of a UAV.

those obtained by modeling blockages as squares (with side length $2a$) in the horizontal plane. There are two extreme cases: (i) the circle is inside and tangent to the square, i.e., $a = r_b$; and (ii) the circle is outside the square and the square intersects the circle, i.e., $a = r_b/\sqrt{2}$. After running all results of square modeling with different values of $a \in [r_b/\sqrt{2}, r_b]$, we find that when $a = 0.85r_b$, the circular modeling is a good approximation of the square modeling. It can be expected that the insights gained from the simpler circular modeling are similar to those from the more complex non-circular modeling.

VI. Application: Optimal Deployment of a Surveillance UAV

In this section, we propose an application of the joint LoS probability on the deployment of an aerial cellular user (i.e., surveillance UAV) for improving the aerial-terrestrial communication quality. Then, we introduce the performance metric to evaluate the importance of the LoS correlation in the UAV deployment, followed by the numerical results.

A. Network Modeling

As shown in Fig. 17, the cellular network consists of randomly distributed terrestrial base stations (TBSs) with height h_T and a UAV with height h_U, where all BSs and the UAV are equipped with omnidirectional antennas. Moreover, we consider that the movable UAV equipped with a camera to monitor a given area. The position of the surveillance UAV is limited due to the limited viewing capability of the camera. Therefore, we assume that the UAV is only allowed to position itself in a target area (i.e., a square with size $2D \times 2D$ as depicted in Fig. 17), where the UAV can effectively monitor the given area. In Fig. 18, we establish a Cartesian coordinate AOB, where the origin O is the center of the target square and the A-axis and the B-axis are parallel or perpendicular to the sides of the square. The horizontal locations of TBSs in AOB coordinate system, denoted by $\mathbf{t}_i$, follow a PPP $\Psi_T = \{\mathbf{t}_i\}$ with density λ_T, where $i = 1, 2, \ldots$ [30]. For tractability, we uniformly discretize the possible horizontal positions of the UAV at the target area into the grid points in Fig. 18. The total number of grid points is J and the locations of the regular grid points form a set $\Psi_G = \{\mathbf{g}_j\}$. Note that $\mathbf{g}_1$, $\mathbf{g}_2$,..., and $\mathbf{g}_J$ are ordered in the direction of the blue arrows in the grids of Fig. 18, i.e., $\mathbf{g}_1 = (0, 0)$ and $\mathbf{g}_J = (-D, -D)$.

B. Optimal Deployment

The UAV for surveillance should be associated with a TBS in the cellular network to upload the observed information. The well-designed position of the UAV is of great importance to ensure the Quality of Service (QoS). When optimizing the position of the UAV, for simplicity, we adopt the widely-used nearest association rule that the UAV is served by its nearest

TBS. Generally, the signal power experiences path loss during transmission, which depends on the transmission distance and the LoS/NLoS conditions. Compared with NLoS transmission, LoS transmission greatly reduces path loss. Hence, to obtain the optimal position of the UAV with the high QoS, we aim at maximizing both the LoS probability between the UAV and its nearest TBS (i.e. its serving TBS) for high received power and the NLoS probability between the UAV and its 2nd-nearest TBS (i.e. its nearest interfering TBS) for low interference. It is worth mentioning that the 2nd-nearest BS with a short-distance path loss to the UAV dominates the interference at the UAV. Moreover, the decreasing gap between the conditional and unconditional LoS probability with θ and D_2 in the A2T setting in Fig. 12 supports the reasonability of the optimization rule, i.e., we only consider the nearest TBS and 2nd-nearest TBS. Namely, we ignore the correlation of the LoS probabilities between the channel from the UAV to the nearest TBS and the channel from the UAV to the 3rd-nearest (or further) TBS by adopting the independence assumption of LoS probabilities between them. Following the modeling in Section III and IV-C, we regard the UAV, its nearest TBS and its 2nd-nearest TBS as Q_0, Q_1 and Q_2, respectively, where $D_2 \geq D_1$. Their horizontal locations are denoted by $\mathbf{q}_0$, $\mathbf{q}_1$, and $\mathbf{q}_2$, respectively, where $\mathbf{q}_0 \in \Psi_{\mathrm{G}}$, and $\mathbf{q}_1, \mathbf{q}_2 \in \Psi_{\mathrm{T}}$. NLoS_2 is the event that there exist a NLoS channel between Q_0 and Q_2, where $\mathbb{P}(\mathrm{NLoS}_2) = 1 - \mathbb{P}(\mathrm{LoS}_2)$. Thus, the optimization problem can be defined as

$$\mathbf{OP}: \max_{\mathbf{g}_j \in \Psi_{\mathrm{G}}} \mathbb{P}(\mathrm{LoS}_1, \mathrm{NLoS}_2). \tag{37}$$

Similar to (6), we consider the correlation between events LoS_1 and NLoS_2. The joint LoS&NLoS probability in (37) can be accurately rewritten as

$$\begin{aligned}\mathbb{P}(\mathrm{LoS}_1, \mathrm{NLoS}_2) &= \mathbb{P}(\mathrm{NLoS}_2|\mathrm{LoS}_1)\mathbb{P}(\mathrm{LoS}_1) \\ &= (1 - \mathbb{P}(\mathrm{LoS}_2|\mathrm{LoS}_1))\,\mathbb{P}(\mathrm{LoS}_1) \\ &= (1 - \mathbb{P}(\mathrm{LoS}_2|\mathrm{LoS}_1))\,\mathbb{P}^*(\mathrm{LoS}_1),\end{aligned} \tag{38}$$

where $\mathbb{P}^*(\mathrm{LoS}_1) = \mathbb{P}(\mathrm{LoS}_1)$ is from $D_2 \geq D_1$. Thus, (37) can be transformed into

$$\mathbf{OP}_1: \max_{\mathbf{g}_j \in \Psi_{\mathrm{G}}} (1 - \mathbb{P}(\mathrm{LoS}_2|\mathrm{LoS}_1))\,\mathbb{P}(\mathrm{LoS}_1). \tag{39}$$

On the other hand, if we assume the independence between events LoS_1 and NLoS_2 as in (7), (37) can be approximated as

$$\mathbf{OP}_2: \max_{\mathbf{g}_j \in \Psi_{\mathrm{G}}} (1 - \mathbb{P}(\mathrm{LoS}_2))\,\mathbb{P}(\mathrm{LoS}_1). \tag{40}$$

We denote the optimal solutions of (39) and (40) as $\mathbf{u}_1$ and $\mathbf{u}_2$, respectively, which can be obtained by Algorithm 1 based on the grid search. Besides, the segments with the arrows in Fig. 18 depict the process of the grid search (staring from (0,0) and ended with $(-D, -D)$). Fig. 18 also presents the initial setup before finding the optimal location by marking the UAV above origin as Q_0, the nearest BS to the origin as Q_1, and the 2nd-nearest BS to the origin as Q_2.

Algorithm 1: Grid Search for Optimal Deployment of a UAV.

1: Input r_{b}, Ψ_{T}, and Ψ_{G}.
2: Set $H_{Q_0} = h_{\mathrm{U}}$ and $H_{Q_1} = H_{Q_2} = h_{\mathrm{T}}$.
3: Initialize $\{\rho_1^j\}$ and $\{\rho_2^j\}$ for recording the accurate or approximate $\mathbb{P}(\mathrm{LoS}_1, \mathrm{NLoS}_2)$.
4: **for** $j = 1$ to J **do**
5: Set the horizontal location of the UAV (Q_0) as $\mathbf{q}_0 = \mathbf{g}_j \in \Psi_{\mathrm{G}}$;
6: Find the nearest TBS (Q_1) to the UAV by $\mathbf{q}_1 = \arg\min_{\mathbf{t}_i \in \Psi_{\mathrm{T}}} ||\mathbf{g}_j - \mathbf{t}_i||$;
7: Find the 2nd-nearest TBS (Q_2) to the UAV by $\mathbf{q}_2 = \arg\min_{\mathbf{t}_i \in \Psi_{\mathrm{T}} \setminus \{\mathbf{q}_1\}} ||\mathbf{g}_j - \mathbf{t}_i||$;
8: Establish the XO_0Y and UO_2V coordinate systems as in Section II and III;
9: Calculate D_1, D_2, and θ;
10: Calculate $\mathbb{P}(\mathrm{LoS}_1)$ and $\mathbb{P}(\mathrm{LoS}_2)$ as in (5);
11: Based on the value of θ, r_{b}, D_1, and D_2, find the corresponding expression in Section IV to calculate $\mathbb{P}(\mathrm{LoS}_2|\mathrm{LoS}_1)$.
12: Record $\rho_1^j = (1 - \mathbb{P}(\mathrm{LoS}_2|\mathrm{LoS}_1))\mathbb{P}(\mathrm{LoS}_1)$ and $\rho_2^j = (1 - \mathbb{P}(\mathrm{LoS}_2))\mathbb{P}(\mathrm{LoS}_1)$.
13: **end for**
14: Set $\mathbf{u}_1 = \arg\max_{\mathbf{g}_j \in \Psi_{\mathrm{G}}} \{\rho_1^j\}$ and $\mathbf{u}_2 = \arg\min_{\mathbf{g}_j \in \Psi_{\mathrm{G}}} \{\rho_2^j\}$.

C. Performance Metric

The coverage probability (i.e., the probability that the signal-to-interference ratio (SIR) is larger than a predefined threshold) can be used as a metric to quantify the communication quality. To evaluate the advantage of the accurate optimization of $\mathbb{P}(\mathrm{LoS}_1, \mathrm{NLoS}_2)$ in (39) than the approximate one in (40), we then analyze the coverage probability of the UAV in downlink (by setting the location of the UAV as $\mathbf{q}_0 = \mathbf{u}_1$ and $\mathbf{q}_0 = \mathbf{u}_2$, respectively).

Based on (5), we further divide the TBSs Ψ_{T} into (i) TBSs with LoS channels to the UAV, denoted by $\Psi_{\mathrm{T,L}}$ and (ii) TBSs with NLoS channels to the UAV, denoted by $\Psi_{\mathrm{T,N}}$, where $\Psi_{\mathrm{T}} = \Psi_{\mathrm{T,L}} \cup \Psi_{\mathrm{T,N}}$ and $\Psi_{\mathrm{T,L}} \cap \Psi_{\mathrm{T,N}} = \varnothing$. The path loss between the UAV located at $\mathbf{q}_0$ and a TBS located at $\mathbf{t}_i \in \Psi_{\mathrm{T},k}$ ($k \in \{\mathrm{L}, \mathrm{N}\}$) is given by

$$\zeta_k(\mathbf{q}_0, \mathbf{t}_i) = \eta_k \left(||\mathbf{q}_0 - \mathbf{t}_i||^2 + (h_{\mathrm{T}} - h_{\mathrm{U}})^2\right)^{\alpha_k/2}, \tag{41}$$

where $||\mathbf{q}_0 - \mathbf{t}_i||$ is the horizontal distance between the transceivers, $k = \mathrm{L}$ refers to LoS transmission for $\mathbf{t}_i \in \Psi_{\mathrm{T,L}}$, $k = \mathrm{N}$ refers to NLoS transmission for $\mathbf{t}_i \in \Psi_{\mathrm{T,N}}$, $\alpha_{\mathrm{L}}/\alpha_{\mathrm{N}}$ is the corresponding LoS/NLoS path-loss index, and $\eta_{\mathrm{L}}/\eta_{\mathrm{N}}$ is the reference path loss when the distance is 1 m. Therefore, the received power is given by

$$P_{\mathrm{r},k}(\mathbf{q}_0, \mathbf{t}_i) = P_{\mathrm{t}} G_{\mathrm{t}} \zeta_k(\mathbf{q}_0, \mathbf{t}_i) \Omega_{k,i}, k \in \{\mathrm{L}, \mathrm{N}\}, \tag{42}$$

where P_{t} is the transmit power of TBSs, G_{t} is the antenna gain, and $\Omega_{k,i}$ is the small-scale fading with $\mathbb{E}[\Omega_{k,i}] = 1$. Specifically, we adopt the Nakagami-m fading model with shaping

parameters m_{L} and m_{N} for the LoS and NLoS transmission, respectively. The probability density function (PDF) of $\Omega_{k,i}$ is given by [31]

$$f_{\Omega_{k,i}}(\omega) = \frac{m_k^{m_k}\omega^{m_k-1}}{\Gamma(m_k)} e^{-m_k\omega}, k = \{\mathrm{L}, \mathrm{N}\}, \quad (43)$$

where $\Gamma(m)$ is the Gamma function and $\Gamma(m) = \int_0^\infty u^{m-1} e^{-u}\mathrm{d}u$ [32].

Different from Section VI-B, we modify the association rule between TBSs and the UAV. We consider that the UAV is associated with the TBS that provides the *strongest average received power*, making the model more suitable for the real implementation scenario [18], [27]. By noting that $\mathbb{E}[\Omega_{k,i}] = 1$, the average received power is given by

$$\bar{P}_{\mathrm{r},k}(\mathbf{q}_0, \mathbf{t}_i) = \mathbb{E}[P_{\mathrm{r},k}(\mathbf{q}_0, \mathbf{t}_i)] = P_{\mathrm{t}} G_{\mathrm{t}} \zeta_k(\mathbf{q}_0, \mathbf{t}_i). \quad (44)$$

It can be seen from (44) that the closest TBS (denoted by $\mathbf{t}_k$) in $\Psi_{\mathrm{T},k}$ provides the strongest average received power among the TBSs in $\Psi_{\mathrm{T},k}$, i.e.,

$$\mathbf{t}_k = \arg \min_{\mathbf{t}_i \in \Psi_{\mathrm{T},k}} ||\mathbf{q}_0 - \mathbf{t}_i||, k = \{\mathrm{L}, \mathrm{N}\}. \quad (45)$$

Hence, the location of the serving TBS, denoted by $\mathbf{t}_0$, is

$$\mathbf{t}_0 = \arg \max_{\mathbf{t}_{\mathrm{L}}, \mathbf{t}_{\mathrm{N}}} \left\{\bar{P}_{\mathrm{r,L}}(\mathbf{q}_0, \mathbf{t}_{\mathrm{L}}), \bar{P}_{\mathrm{r,N}}(\mathbf{q}_0, \mathbf{t}_{\mathrm{N}})\right\}. \quad (46)$$

With the serving TBS $\mathbf{t}_0$, the aggregate interference is

$$I(\mathbf{q}_0, \mathbf{t}_0) = \sum_{\mathbf{t}_i \in \Psi_{\mathrm{T,L}} \setminus \{\mathbf{t}_0\}} P_{\mathrm{r,L}}(\mathbf{q}_0, \mathbf{t}_i) + \sum_{\mathbf{t}_i \in \Psi_{\mathrm{T,N}} \setminus \{\mathbf{t}_0\}} P_{\mathrm{r,N}}(\mathbf{q}_0, \mathbf{t}_i). \quad (47)$$

Therefore, the instantaneous SIR is given by

$$\mathrm{SIR}(\mathbf{q}_0, \mathbf{t}_0) = \frac{P_{\mathrm{r},k}(\mathbf{q}_0, \mathbf{t}_0)}{I(\mathbf{q}_0, \mathbf{t}_0)}, \quad (48)$$

where k depends on (46), i.e., whether $\mathbf{t}_0 = \mathbf{t}_{\mathrm{L}}$ or $\mathbf{t}_0 = \mathbf{t}_{\mathrm{N}}$. Given the threshold τ, we define the coverage probability as

$$\mathcal{P}^{\mathrm{cov}} = \mathbb{P}[\mathrm{SIR}(\mathbf{q}_0, \mathbf{t}_0) > \tau]. \quad (49)$$

D. Numerical Results

The optimal deployment of the UAV is conducted based on the accurate and approximate joint LoS&NLoS probability in (39) and (40), respectively. By running Algorithm 1, we obtain two optimized positions of the UAV, i.e., $\mathbf{u}_1$ and $\mathbf{u}_2$. In this subsection, we first present the difference in the accurate joint LoS&NLoS probabilities when the UAV is placed at $\mathbf{u}_1$ and $\mathbf{u}_2$, respectively. Then, we compare the coverage probabilities of the UAV at $\mathbf{u}_1$ and the UAV at $\mathbf{u}_2$. The default values of model parameters are given in Table IV.

Fig. 19(a) provides the normalized improvement on the joint LoS&NLoS probability by comparing the optimization in (39) with that in (40). Specifically, assuming the UAV at $\mathbf{u}_1$ and $\mathbf{u}_2$, we denote the accurate joint LoS&NLoS probability $\mathbb{P}(\mathrm{LoS}_1, \mathrm{NLoS}_2)$ in (38) as $\mathrm{P}_{\mathrm{u}_1}$ and $\mathrm{P}_{\mathrm{u}_2}$, respectively. The normalized improvement, denoted by $\mathrm{P}_{\mathrm{imp}}$, on $\mathbb{P}(\mathrm{LoS}_1, \mathrm{NLoS}_2)$ can be expressed as $\mathrm{P}_{\mathrm{imp}} = (\mathrm{P}_{\mathrm{u}_1} - \mathrm{P}_{\mathrm{u}_2})/\mathrm{P}_{\mathrm{u}_1}$. From Fig. 19(a), the non-zero value of $\mathrm{P}_{\mathrm{imp}}$ indicates that the solutions of two optimization problems (39) and (40) are different; the positive value of $\mathrm{P}_{\mathrm{imp}}$ indicates that the optimization in (39) is better than that in (40) with respect to the accurate joint LoS&NLoS probability $\mathbb{P}(\mathrm{LoS}_1, \mathrm{NLoS}_2)$. Additionally, there is an increasing tendency of $\mathrm{P}_{\mathrm{imp}}$ when we decrease the UAV height h_{U} or increase the blockage density λ_{b}. In fact, the lower height of the UAV and denser blockages correspond to the higher probability of NLoS channels. This observation shows the importance of the LoS correlation, especially in a highly blocked communication environment.

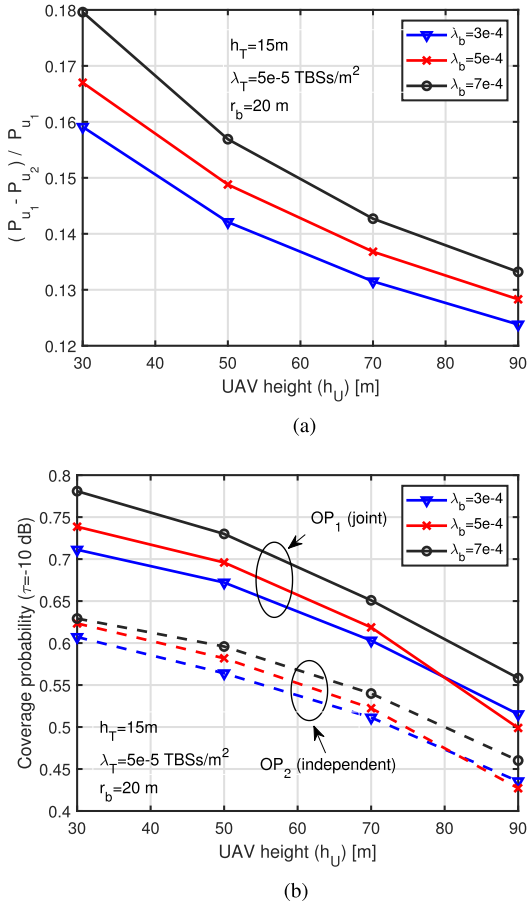

Fig. 19. Optimal deployment of the UAV vs UAV height, for different blockage densities. (a) Normalized improvement on $\mathbb{P}(\mathrm{LoS}_1, \mathrm{NLoS}_2)$. (b) Coverage probability.

In Fig. 19(b), we present coverage probabilities in (49) of the UAV located at $\mathbf{u}_1$ and $\mathbf{u}_2$ vs UAV height, for different blockage densities. We see that the optimization of the UAV position based on (39) exhibits a significantly higher coverage probability than that on (40). Namely, applying our modeling into the deployment of the UAV ensures not only the accuracy of analysis but also the high QoS of the UAV. Fig. 19(b) also reveals the impact of the UAV height h_{U} and the blockage density on the coverage probability. The higher the UAV, the lower the coverage probability. In general, the coverage probability

decreases as h_{U} increases due to the higher probability of LoS transmission on the interfering channels and the long distance of the serving channel, finally reducing the SIR at the UAV. On the other hand, the denser blockages result in the reduced LoS probabilities of the serving link (negatively impacting SIR) and the interfering link (positively impacting SIR). However, the UAV can move to another position to build a LoS connection with a new transmitter, compensating for the negative impact of increasing λ_b to some extent. This explains why there is an increase in the coverage probability as λ_b increases when $h_{\mathrm{U}} \leq 70\,\mathrm{m}$. While the degradation in coverage performance can be observed at $h_{\mathrm{U}} = 90\,\mathrm{m}$ when we increase λ_{b} from 3×10^{-4} to $5 \times 10^{-4}\,\mathrm{blockages}/\mathrm{m}^2$. In this case, the detrimental effect of the increased blockage density outweighs its benefit.

VII. Conclusion

In this paper, we propose a 3D geometrical modeling of the joint LoS probability that both channels (among three communication devices) are not obstructed by the blockages, which considers the correlation of the LoS conditions between channels, i.e., LoS_1 and LoS_2. Using tools of stochastic geometry, we model the blockages as cylinders with random heights. We derive the exact expressions of the conditional and joint LoS probabilities and validate them by Monte Carlo simulations. The numerical results show the correlation between LoS_1 and LoS_2, especially when communication devices are close to each other. Moreover, channel parameters (e.g., the distance, included angle, the heights of communication devices) and environment parameters (e.g., the size, height and density of the blockages) can be adjusted to apply for various scenarios. We also demonstrate that cylindrical blockages serve as a suitable model to approximate non-cylindrical blockages. The accurate characterization of the LoS correlation can be useful in designing the aerial-terrestrial communication system. For example, we optimize the deployment of a UAV based on the correlation of the LoS probabilities between the serving channel and the interfering channel. The improved coverage probability of the UAV verifies the effectiveness of our model in the deployment of the UAV.

References

[1] X. Wang et al., "Millimeter wave communication: A comprehensive survey," *IEEE Commun. Surv. Tut.*, vol. 20, no. 3, pp. 1616–1653, thirdquarter 2018.

[2] S. K. Khan, U. Naseem, H. Siraj, I. Razzak, and M. Imran, "The role of unmanned aerial vehicles and mmWave in 5G: Recent advances and challenges," *Trans. Emerg. Telecommun. Technol.*, vol. 32, no. 7, 2021, Art. no. e4241.

[3] J. G. Andrews, T. Bai, M. N. Kulkarni, A. Alkhateeb, A. K. Gupta, and R. W. Heath, "Modeling and analyzing millimeter wave cellular systems," *IEEE Trans. Commun.*, vol. 65, no. 1, pp. 403–430, Jan. 2017.

[4] A. K. Gupta, J. G. Andrews, and R. W. Heath, "Impact of correlation between link blockages on macro-diversity gains in mmWave networks," in *Proc. IEEE Int. Conf. Commun. Workshops*, Kansas City, MO, USA, 2018, pp. 1–6.

[5] S. K. Gupta, V. Malik, A. K. Gupta, and J. G. Andrews, "Impact of blocking correlation on the performance of mmWave cellular networks," *IEEE Trans. Commun.*, vol. 70, no. 7, pp. 4925–4939, Jul. 2022.

[6] Y. Zeng, Q. Wu, and R. Zhang, "Accessing from the sky: A tutorial on UAV communications for 5G and beyond," *Proc. IEEE*, vol. 107, no. 12, pp. 2327–2375, Dec. 2019.

[7] Q. Wu, S. Zhang, B. Zheng, C. You, and R. Zhang, "Intelligent reflecting surface-aided wireless communications: A tutorial," *IEEE Trans. Commun.*, vol. 69, no. 5, pp. 3313–3351, May 2021.

[8] M. A. Kishk and M.-S. Alouini, "Exploiting randomly located blockages for large-scale deployment of intelligent surfaces," *IEEE J. Sel. Areas Commun.*, vol. 39, no. 4, pp. 1043–1056, Apr. 2021.

[9] A. Al-Hourani, S. Kandeepan, and S. Lardner, "Optimal LAP altitude for maximum coverage," *IEEE Wireless Commun. Lett.*, vol. 3, no. 6, pp. 569–572, Dec. 2014.

[10] A. A. Deshpande, A. Zanella, R. Pereira, A. Pastore, X. Mestre, and F. Chiariotti, "Beam aware stochastic multihop routing for flying ad-hoc networks," in *Proc. IEEE Int. Conf. Commun. Workshops*, Seoul, Korea, 2022, pp. 1065–1070.

[11] Y. Hmamouche, M. Benjillali, and S. Saoudi, "Terrestrial connectivity through constellations of high altitude platform station (HAPS)," in *Proc. Int. Symp. Signal, Image, Video Commun.*, El Jadida, Morocco, 2022, pp. 1–6.

[12] A. Al-Hourani, "On the probability of line-of-sight in urban environments," *IEEE Wireless Commun. Lett.*, vol. 9, no. 8, pp. 1178–1181, Aug. 2020.

[13] E. Access, "Further advancements for E-UTRA physical layer aspects," 3rd Generation Partnership Project, Sophia Antipolis, France, Technical Specification TR, 3GPP TR 36.814 V.9.0.0, Release 9, Mar. 2010.

[14] P. Series, "Propagation Data and Prediction Methods Required for the Design of Terrestrial Broadband Radio Access Systems Operating in a Frequency Range From 3 to 60GHz," ITU-R Standard P.1410, Recommendation International Telecommunication Union, Geneva, Switzerland, 2013.

[15] S. Kandeepan, K. Gomez, L. Reynaud, and T. Rasheed, "Aerial-terrestrial communications: Terrestrial cooperation and energy-efficient transmissions to aerial base stations," *IEEE Trans. Aerosp. Electron. Syst.*, vol. 50, no. 4, pp. 2715–2735, Oct. 2014.

[16] D. Cvitanić, "Drone applications in transportation," in *Proc. Int. Conf. Smart Sustain. Technol.*, Split, Croatia, 2020, pp. 1–4.

[17] M. Mozaffari, W. Saad, M. Bennis, Y.-H. Nam, and M. Debbah, "A tutorial on UAVs for wireless networks: Applications, challenges, and open problems," *IEEE Commun. Surv. Tut.*, vol. 21, no. 3, pp. 2334–2360, thirdquarter 2019.

[18] L. Chen, M. A. Kishk, and M.-S. Alouini, "Dedicating cellular infrastructure for aerial users: Advantages and potential impact on ground users," *IEEE Trans. Wireless Commun.*, vol. 22, no. 4, pp. 2523–2535, Apr. 2023.

[19] D. He, B. Ai, K. Guan, L. Wang, Z. Zhong, and T. Kürner, "The design and applications of high-performance ray-tracing simulation platform for 5G and beyond wireless communications: A tutorial," *IEEE Commun. Surv. Tut.*, vol. 21, no. 1, pp. 10–27, Firstquarter 2019.

[20] M. A. Kishk, A. Bader, and M.-S. Alouini, "On the 3-D placement of airborne base stations using tethered UAVs," *IEEE Trans. Commun.*, vol. 68, no. 8, pp. 5202–5215, Aug. 2020.

[21] M. Matracia, M. A. Kishk, and M.-S. Alouini, "Coverage analysis for UAV-assisted cellular networks in rural areas," *IEEE Open J. Veh. Technol.*, vol. 2, pp. 194–206, 2021.

[22] M. Kishk, A. Bader, and M.-S. Alouini, "Aerial base station deployment in 6G cellular networks using tethered drones: The mobility and endurance tradeoff," *IEEE Veh. Technol. Mag.*, vol. 15, no. 4, pp. 103–111, Dec. 2020.

[23] A. Al-Hourani, S. Kandeepan, and A. Jamalipour, "Modeling air-to-ground path loss for low altitude platforms in urban environments," in *Proc. IEEE Glob. Commun. Conf.*, Austin, TX, USA, 2014, pp. 2898–2904.

[24] Z. Cui, K. Guan, C. Briso-Rodríguez, B. Ai, and Z. Zhong, "Frequency-dependent line-of-sight probability modeling in built-up environments," *IEEE Internet Things J.*, vol. 7, no. 1, pp. 699–709, Jan. 2020.

[25] Q. Zhu et al., "Geometry-based stochastic line-of-sight probability model for A2G channels under urban scenarios," *IEEE Trans. Antennas Propag.*, vol. 70, no. 7, pp. 5784–5794, Jul. 2022.

[26] M. M. Azari, F. Rosas, and S. Pollin, "Reshaping cellular networks for the sky: Major factors and feasibility," in *Proc. IEEE Int. Conf. Commun.*, Kansas City, MO, USA, 2018, pp. 1–7.

[27] M. Alzenad and H. Yanikomeroglu, "Coverage and rate analysis for vertical heterogeneous networks (VHetNets)," *IEEE Trans. Wireless Commun.*, vol. 18, no. 12, pp. 5643–5657, Dec. 2019.

[28] S. Aditya, H. S. Dhillon, A. F. Molisch, and H. M. Behairy, "A tractable analysis of the blind spot probability in localization networks under correlated blocking," *IEEE Trans. Wireless Commun.*, vol. 17, no. 12, pp. 8150–8164, Dec. 2018.
[29] S. Aditya, H. S. Dhillon, A. F. Molisch, and H. Behairy, "Asymptotic blind-spot analysis of localization networks under correlated blocking using a Poisson line process," *IEEE Wireless Commun. Lett.*, vol. 6, no. 5, pp. 654–657, Oct. 2017.
[30] M. Haenggi, *Stochastic Geometry for Wireless Networks.* Cambridge, U.K.: Cambridge Univ. Press, 2012.
[31] M. K. Simon and M.-S. Alouini, *Digital Communication Over Fading Channels*, vol. 95. Hoboken, NJ, USA: Wiley, 2005.
[32] P. J. Davis, "Leonhard euler's integral: A historical profile of the gamma function: In Memoriam: Milton Abramowitz," *Amer. Math. Monthly*, vol. 66, no. 10, pp. 849–869, 1959.

Lin Chen (Graduate Student Member, IEEE) received the B.S. degree in communication engineering from the University of Electronic Science and Technology of China, Chengdu, China, in 2022. From 2021 to 2022, she was a Visiting Student with the King Abdullah University of Science and Technology, Thuwal, Saudi Arabia. She is currently working toward the Ph.D. degree with the Department of Information Engineering, The Chinese University of Hong Kong, Hong Kong. Her research interests include stochastic geometry, mmWave, and RIS for wireless communications.

Wentao Zhang received the bachelor's degree in electronic information engineering in 2021. He studied with the University of Electronic Science and Technology of China, Chengdu, China. His research focuses on wireless communication.

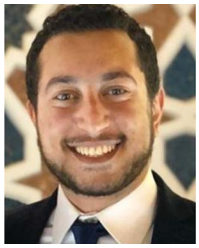

Mustafa A. Kishk (Member, IEEE) received the B.Sc. and M.Sc. degrees in electrical engineering from Cairo University, Giza, Egypt, in 2013 and 2015, respectively, and the Ph.D. degree in electrical engineering from Virginia Tech, Blacksburg, VA, USA, in 2018. He is currently an Assistant Professor with the Electronic Engineering Department, Maynooth University, Ireland. Before that, he was a Postdoctoral Research Fellow with the Communication Theory Laboratory, King Abdullah University of Science and Technology, Thuwal, Saudi Arabia. He is currently an Associate Editor with IEEE WIRELESS COMMUNICATION LETTERS. His current research interests include stochastic geometry, UAV-enabled communication systems, and satellite-enabled communications. He was the recipient of the IEEE ComSoc Outstanding Young Researcher Award for Europe, Middle East, and Africa Region, in 2022. He was recognized as an Exemplary Reviewer by the IEEE Communications Letters in 2020 and 2021.

Mohamed-Slim Alouini (Fellow, IEEE) was born in Tunis, Tunisia. He received the Ph.D. degree in electrical engineering from California Institute of Technology (Caltech), Pasadena, CA, USA, in 1998. He was a Faculty Member with the University of Minnesota, Minneapolis, MI, USA, then with Texas A&M University at Qatar, Ar-Rayyan, Qatar, before joining the King Abdullah University of Science and Technology, Thuwal, Saudi Arabia, as a Professor of electrical engineering in 2009. His current research interests include the modeling, design, and performance analysis of wireless communication systems.